

Emergence and tunability of Fermi-pocket and electronic instabilities in layered Nickelates

Alpesh SHETH¹, Claudine LACROIX², Sébastien BURDIN¹

¹ Université de Bordeaux, CNRS, LOMA, UMR 5798, 33400 Talence, France.

² Institut Néel, CNRS and Université Grenoble-Alpes, Boite Postale 166, 38042 Grenoble Cedex 09, France.

E-mail: alpeshsheth.phy@gmail.com

Abstract.

Layered Nickelates have gained intensive attention as potential high-temperature superconductors, showing similarities and subtle differences to well-known Cuprates. This study introduces a modelling framework to analyze the tunability of electronic structures by focusing on effective orbitals and additional Fermi pockets, mimicking doping or external pressure qualitatively. It investigates the role of the $3d_{z^2}$ orbital in interlayer hybridization, which leads to the formation of a second pocket in the Fermi surface. The resulting effective model also predicts specific charge and spin susceptibility in the form of Lindhard susceptibility at wave vector $\mathbf{q}_0 = (\pi, \pi)$, which can be tuned by doping or pressure. These results provide valuable insights into tunable orbital contributions and their influence on potential ordering and electronic instabilities in Layered Nickelates.

1. Introduction

The discovery of superconductivity in hole-doped layered Nickelates such as $RNiO_2$ ($R = \text{La, Nd, Pr}$) [1, 2, 3, 4, 5, 6] has led to extensive studies into their electronic and magnetic properties and potential pairing mechanisms. These studies often compare layered Nickelates with relatively well-studied Cuprates. Despite similar structure and isoelectronic configurations of $Ni^{1+} : 3d^9$, layered Nickelates have subtle distinctions compared to Cuprates, such as dependence on the synthesis method, the role of 3-dimensionality [7], debatable charge order [8, 9], questionable magnetic behavior [1, 5, 10, 11, 12, 13, 14, 15], and the possible presence and origin of a second pocket in Fermi surface [16, 17, 18, 19, 20, 21, 22, 23, 24].

Typically, studies of these distinctions focus on the superconductivity of layered Nickelates or emphasize the differences between layered Nickelates and Cuprates. Rarely do they explore how specific synthesis steps, such as removing apical Oxygen, layer formation, doping, or applying external pressure, affect the electronic structure and instabilities. One alternative approach to understand these distinctions is to examine

the changes in electronic structure and instabilities during the stoichiometric reduction from its parent compound, the perovskite Nickelates ($RNiO_3$). In a broader context, the parent perovskite Nickelates themselves are known for their rich electronic and magnetic properties, including metal-insulator transitions (MIT), charge ordering, novel magnetic phases, and bond disproportionation [25, 26, 27, 28, 29, 30, 31]. However, the specific mechanisms driving those aforementioned phenomena in perovskite Nickelates are still under active investigation [29, 30]. Furthermore, perovskite [32, 33, 34] and layered Nickelates [35, 36, 37, 38, 39] exhibit competing electronic instabilities confirmed by various experimental and theoretical studies, but there are no reports of superconductivity in perovskite Nickelates.

Scrutinizing the orbital contribution in perovskite and layered Nickelates, Angle-Resolved Photoemission Spectroscopy (ARPES) studies on $RNiO_3$ ($R = La, Nd$) reveal the $3d_{x^2-y^2}$ and $3d_{z^2}$ orbitals to be the primary dominant contributors to the Fermi surface in perovskite Nickelates [40, 41]. Meanwhile, ARPES measurements [16, 17, 42, 43] of layered Nickelates show contribution only from the $3d_{x^2-y^2}$ orbital. On the other hand, several DFT-based tight-binding models on layered Nickelates have captured two pockets in the Fermi surface [23, 44, 45, 46, 47, 48, 49, 50, 51, 15, 52, 20]. The orbital origin of one of these two pockets is consistently recognized to be the $3d_{x^2-y^2}$ orbital, while the presence and origin of the second pocket is a topic of non-consensus. Such non-consensus is also present in the potential role of order (magnetic or charge) [8, 9, 35] in layered Nickelates. On the theoretical side, there are attempts to include interaction effects in layered Nickelates that range from Mott, Hubbard, and Hund physics [22, 53, 54, 55, 56, 57, 58]. These approaches typically use methods beyond Density Functional Theory (DFT) [59, 15, 46, 60], such as Dynamical Mean Field Theory (DMFT) [51, 23] and Dynamical Vertex Approximation [51, 61]. We recognize the importance of correlations in layered nickelates. However, this study specifically focuses on two key issues: (1) the emergence and tunability of a second pocket in the Fermi surface, and (2) the development of electronic charge or spin instabilities. These phenomena can be experimentally manifested by doping or applying external pressure.

The paper is structured as follows: Section (2) introduces a comprehensive framework for modeling Nickelate structures with a focus on layered Nickelates. We begin by analyzing the orbital symmetries based on the paramagnetic normal states of well-established, undistorted cubic perovskite Nickelates, and apply these findings to layered Nickelates. We then deduce key orbital degrees of freedom and hybridization effects that can either be neglected or absorbed into the effective tight-binding parameters. This leads us to an effective model for layered Nickelates, which sheds light on the tunability of the Fermi surface. Section (3) complements this framework by providing static susceptibility calculations that offer insights into potential ordering phenomena and instabilities within the system.

2. General Model

Various effective models based on DFT and Wannierization have been developed to capture complex electronic structures of layered Nickelates $RNiO_2$. Some of these models utilize up to 17 orbitals to fit the band structure of $RNiO_2$, incorporating contributions from Nickel $3d$ -orbitals, Rare-earth $5d$ -orbitals, Oxygen $2p$ -orbitals, and an interstitial s -orbital [44, 62]. To simplify these models, reductions to four orbitals (such as $3d_{x^2-y^2}$, interstitial s , $5d_{z^2}$, and $5d_{xy}$) [44, 62], three orbitals (including $3d_{x^2-y^2}$, $3d_{z^2}$, and a self-doping orbital) [63, 64, 23], two orbitals ($3d_{x^2-y^2}$ and an interstitial s -orbital) [45], or even a single-orbital effective model based on $3d_{x^2-y^2}$ [51] have been proposed. However, in this work, we consider the already established orbital symmetry of perovskite Nickelates and deduce the relevant effective orbital responsible for the emergence of an extra Fermi pocket in Layered Nickelates.

In section 2.1 we develop generalized modelling framework from multi-orbital description of $RNiO_n$, followed by a specific case of layered Nickelates in section 2.2. Based on the inferences from the relevant symmetries, orbitals and parameters in section 2.3, we propose an effective model capturing trends of the multi-orbital description of layered Nickelates. However, it is to note that the adaptation of this modelling framework can be more general, for example, in Supplementary, where it is qualitatively adapted for 3-Dimensional $RNiO_3$.

2.1. Multi-orbital description of $RNiO_n$

In this section, we introduce the generalized Hamiltonian formalism for capturing the multi-orbital characteristics of the $RNiO_n$ system, which has N orbitals per site representing atomic orbitals of R , Ni , and O . The non-interacting Hamiltonian, expressed as a block matrix, comprehensively accounts for the electronic structure within a multi-orbital framework.

The Hamiltonian \mathcal{H} is given by the following equation:

$$\mathcal{H} = \sum_{\sigma} \sum_i \Psi_i^{\dagger\sigma} \tilde{\mathcal{E}}_0 \Psi_i^{\sigma} + \sum_{\sigma} \sum_{\langle ij \rangle} \Psi_i^{\dagger\sigma} \mathbf{T}_{ij} \Psi_j^{\sigma} \quad (1)$$

where the basis set $\Psi_i^{\dagger\sigma}$ (Ψ_i^{σ}) is a row (column) matrix with elements being the creation (annihilation) operators $c_i^{\dagger\alpha\sigma}$ ($c_i^{\alpha\sigma}$) for the orbitals $\alpha \in \{R, Ni, O\}$ and spin $\sigma = \{\uparrow, \downarrow\}$ at site i (see Fig. 1). Here, \mathbf{T}_{ij} is the hopping matrix between sites i and j ; $\tilde{\mathcal{E}}_0$ is the on-site energy, which includes diagonal elements \mathcal{E}_0 and off-diagonal elements $\Delta\mathcal{E}_0$, leading to $\tilde{\mathcal{E}}_0 = \mathcal{E}_0 + \Delta\mathcal{E}_0$.

Although the three-dimensional (tetragonal) description is crucial for understanding Nickelates, we adopt a two-dimensional (2D) description inspired by Cuprates. This 2D system considers a NiO_n layer coupled to a single rare-earth layer, providing a simplified description that still captures some essential features of the three-dimensional system. This system description can still consider some physical ingredients of a three-dimensional system where the interlayer coupling involves only tunnelling along

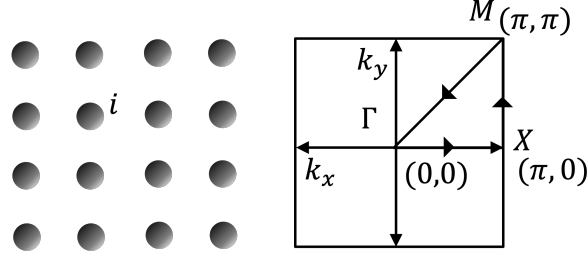


Figure 1: Representative lattice site i and corresponding Brillouin zone in 2D case. In perovskite Nickelates, lattice site i consists of a Rare Earth and a Nickel atom with 3 Oxygen atoms. In layered Nickelates, lattice site i consists of a Rare Earth and a Nickel atom with 2 Oxygen atoms.

the direction between Ni and R orbitals (see supplementary for three-dimensional description).

In momentum space, the Hamiltonian in Eq. (1) can be rewritten as:

$$\mathcal{H} = \sum_{\sigma} \sum_{\mathbf{k}} \Psi_{\mathbf{k}}^{\dagger\sigma} (\mathcal{E}_0 + \mathcal{E}_{\mathbf{k}}) \Psi_{\mathbf{k}}^{\sigma} , \quad (2a)$$

$$\mathcal{E}_{\mathbf{k}} = \Delta\mathcal{E}_0 + \sum_{\delta} \mathbf{T}_{\delta} e^{i\mathbf{k}\cdot\delta}, \quad (2b)$$

where, the summation over \mathbf{k} spans the entire Brillouin zone corresponding to the 2D model. The term $\mathcal{E}_{\mathbf{k}}$ encapsulates both the off-diagonal on-site terms $\Delta\mathcal{E}_0$ and the inter-site hopping terms $\mathbf{T}_{\delta} e^{i\mathbf{k}\cdot\delta}$, where the summation over δ covers the nearest-neighbor contributions.

In a more convenient representation, dispersion $\mathcal{E}_{\mathbf{k}}$ is,

$$\mathcal{E}_{\mathbf{k}} = \begin{bmatrix} \tilde{\varepsilon}_{\mathbf{k}}^R & \tilde{\varepsilon}_{\mathbf{k}}^{RNi} & \tilde{\varepsilon}_{\mathbf{k}}^{RO} \\ \hline \tilde{\varepsilon}_{\mathbf{k}}^{NiR} & \tilde{\varepsilon}_{\mathbf{k}}^{Ni} & \tilde{\varepsilon}_{\mathbf{k}}^{NiO} \\ \hline \tilde{\varepsilon}_{\mathbf{k}}^{OR} & \tilde{\varepsilon}_{\mathbf{k}}^{ONi} & \tilde{\varepsilon}_{\mathbf{k}}^O \end{bmatrix}. \quad (3)$$

The dispersion matrix, $\tilde{\varepsilon}_{\mathbf{k}}^{AB}$, consists of elements that are matrices of size $N_A \times N_B$, where A and B represent atomic species, such as R , Ni , and O . These blocks represent either intra-atomic interactions $\tilde{\varepsilon}_{\mathbf{k}}^A$ or inter-atomic interactions $\tilde{\varepsilon}_{\mathbf{k}}^{AB}$. The overall dispersion matrix, $\mathcal{E}_{\mathbf{k}}$, is constructed from these blocks to form a larger matrix of size $N \times N$, where $N = N_R + N_{Ni} + N_O$ represents the total number of degrees of freedom from all the atomic species and hence the total number of orbitals involved.

The dispersion matrix elements are influenced by the symmetry of the orbitals and the overlap integrals. Once the dispersion $\mathcal{E}_{\mathbf{k}}$ is known, various electronic properties can

be calculated using Green's function formalism, focusing on the paramagnetic state. The Green's function is defined as $\mathcal{G}_{\mathbf{k}}^{\sigma\sigma'}(\tau) = -\langle \Psi_i^\sigma(\tau) \Psi_j^{\dagger\sigma'}(0) \rangle$ and its Fourier transform is given by $\mathcal{G}_{\mathbf{k}}^{\sigma\sigma'}(\omega) = \int d\tau e^{i\omega\tau} \mathcal{G}_{\mathbf{k}}^{\sigma\sigma'}(\tau)$. In paramagnetic case the Green's function is spin diagonal, given by $\mathcal{G}_{\mathbf{k}}^{\sigma\sigma'}(\omega) = \delta_{\sigma\sigma'} \mathcal{G}_{\mathbf{k}}(\omega)$, indicating spin-rotation invariance. Hereafter, we will denote the Green's function as $\mathcal{G}_{\mathbf{k}}(\omega)$, without the spin indices $\sigma\sigma'$ for the sake of clarity. This function is given by $\mathcal{G}_{\mathbf{k}}(\omega) = (\omega - \mathcal{E}_0 - \mathcal{E}_{\mathbf{k}})^{-1}$, where $\mathcal{E}_{\mathbf{k}}$ is given by Eq. (3) and \mathcal{E}_0 is a constant energy.

We can obtain the spectral function $\mathcal{A}_{\mathbf{k}}(\omega)$ and Density of States (DoS) $\rho(\omega)$ from the imaginary part of the trace of Green's function matrix as,

$$\mathcal{A}_{\mathbf{k}}(\omega) = \frac{-1}{\pi} \text{Im} \text{Tr}(\mathcal{G}_{\mathbf{k}}(\omega + i0^+)), \quad (4a)$$

$$\rho(\omega) = \sum_{\mathbf{k}} \mathcal{A}_{\mathbf{k}}(\omega). \quad (4b)$$

Above Eq. (4a) determines the Fermi surface (sharp peaks at the Fermi energy), and Eq. (4b) determines the density of states (DoS). Thus, by analyzing the spectral function, Fermi surface, and DoS obtained from the Green's function formalism for the generalized Hamiltonian defined by Eq. (3), we can gain valuable insights into the electronic structure of $RNiO_n$ system.

Our focus is solely on the electronic characteristics of $RNiO_n$, setting aside structural complexities (such as orthorhombic distortion, bond deformation, and disproportionation). Further exploiting the octahedral crystal field symmetry where the e_g states are higher in energy than t_{2g} states (implying that t_{2g} states are always filled) and do not play a role near the Fermi surface, we yield relatively minimalistic description applicable to layered Nickelates $RNiO_2$ discussed hereafter.

2.2. 4-orbital description of $RNiO_2$

In the process of reducing $RNiO_3$ to $RNiO_2$, the apical Oxygen is removed, resulting in the formation of a layered Nickelate phase. The $RNiO_2$ phase has a square planar symmetry with alternating layers of rare-earth R and NiO_2 stacked along the crystallographic c -axis. The transition from $RNiO_3$ to $RNiO_2$ involves a meta-stable state with a tetragonally distorted octahedral geometry, which influences the electronic structure by lifting the orbital degeneracy in the Nickel $3d$ -orbitals. This leads to a specific energy ordering [65] $\tilde{\epsilon}_{3d_{xz}} = \tilde{\epsilon}_{3d_{yz}} < \tilde{\epsilon}_{3d_{xy}} < \tilde{\epsilon}_{3d_{z^2}} < \tilde{\epsilon}_{3d_{x^2-y^2}}$ in $RNiO_2$. The non-degenerate $\tilde{\epsilon}_{3d_{z^2}} < \tilde{\epsilon}_{3d_{x^2-y^2}}$ in $RNiO_2$ along with non-magnetic metallic nature suggests $3d^9$ ground state. More precisely a composite ground state involves both $3d^9$ and $3d^8 R$ (R is rare-earth) as suggested by experiments such as *O K-edge XAS* [15]. Further, controversy about where the doped holes go upon doping (to $d^9 \underline{L}$ or d^8) [66] leads to the necessity of inclusion of Oxygen orbitals in the proposed model. Since the Nickelates have large $\Delta_{dp} = \tilde{\epsilon}_d - \tilde{\epsilon}_{2p}$ [46, 15, 46] compared to Cuprates and perovskites Nickelates, it is plausible that, this property could also be exploited in modelling them.

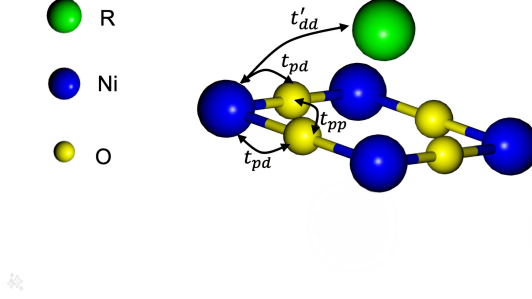


Figure 2: Schematic of in-plane and out-plane hopping parameter in $RNiO_2$

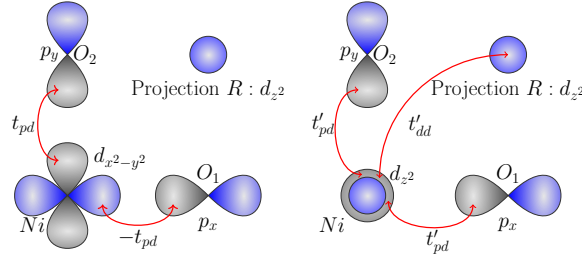


Figure 3: Orbital overlaps and the hopping parameter considering the orbital symmetry of $RNiO_n$ and the in-plane Oxygen atoms O_1 and O_2 .

Thus, as noted earlier in layered Nickelates $3d_{x^2-y^2}$ and $3d_{z^2}$ lie near Fermi-level similar to perovskite Nickelates [40] and Cuprates. Further, both parent perovskite and layered Nickelates have approximately similar e_g bandwidth of 3 eV [67, 68, 69, 70, 21]. In perovskite nickelates, the bandwidth decreases with confinement, leading to an increased charge transfer gap Δ_{d-p} . This is associated with the shrinking ionic radius of R due to Lanthanide Contraction with increasing atomic number and an expanding lattice mismatch on which the layer is grown [67, 68, 69, 70]. Conversely, in $RNiO_2$, the bandwidth consistently expands across the Lanthanide series. Thus, such rare-earth doping is attributed to a reduction in both in-plane [71] and inter-plane [21] lattice constants in layered Nickelates, leading to increased orbital overlap, hybridization, and overall bandwidth. A recent development in the debate about questioning the necessity of $3d_{z^2}$ orbital to describe superconductivity focuses primarily on the $3d_{x^2-y^2}$ orbital [43] supported by ARPES measurement. However, the energetically high-spin scenario is more favourable than the low-spin scenario when transitioning from $d^9 \rightarrow d^8$ [72]. This implies that out of two channels (in-plane within NiO_2 layer or inter-plane through Rare-earth layer), there could be competition which leads to the emergence of a second pocket [1, 2, 3, 4, 5, 6].

To initiate examination of this competition and tunability, we draw analogies from orbital symmetry of related perovskite Nickelates and consider $5d_{z^2}$, $3d_{x^2-y^2}$, $3d_{z^2}$, $2p_x$ and $2p_y$ orbitals. The 2D orbital overlap of these orbitals is as depicted in Fig. 3.

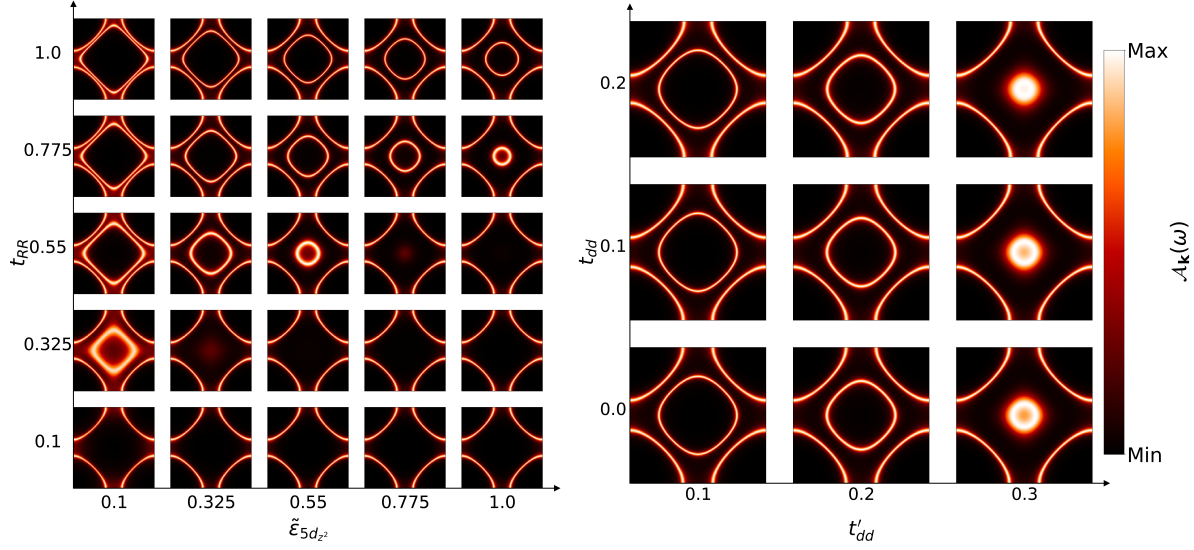


Figure 4: Fermi surface evolution when $\tilde{\varepsilon}_{3d_{z^2}} = -1.5 \text{ eV}$ and $\tilde{\varepsilon}_{3d_{x^2-y^2}} = -1.0 \text{ eV}$ in $RNiO_2$. Left Panel: Varying t_{RR} and $\tilde{\varepsilon}_{5d_{z^2}}$ for a fixed $t'_{dd} = 0.2 \text{ eV}$. Right panel: Varying t'_{dd} and t_{dd} for a fixed $t_{RR} = 0.775 \text{ eV}$ and $\tilde{\varepsilon}_{5d_{z^2}} = 0.55 \text{ eV}$. Each Fermi-surface extend from $-\pi$ to π in (k_x, k_y) plane.

Therefore, using the Hamiltonian Eq. (2) we get blocks in Eq. (3) as,

$$\tilde{\varepsilon}_{\mathbf{k}}^O = \tilde{\varepsilon}_{2p} + \begin{bmatrix} 0 & t_{pp}s_{k_x}s_{k_y}^* \\ t_{pp}s_{k_x}^*s_{k_y} & 0 \end{bmatrix}, \quad (5a)$$

$$\tilde{\varepsilon}_{\mathbf{k}}^{NiO} = \begin{bmatrix} -t'_{pd}s_{k_x} & -t'_{pd}s_{k_y} \\ t_{pd}s_{k_x} & -t_{pd}s_{k_y} \end{bmatrix}, \quad (5b)$$

$$\tilde{\varepsilon}_{\mathbf{k}}^{Ni} = \begin{bmatrix} \tilde{\varepsilon}_{3d_{z^2}} & 0 \\ 0 & \tilde{\varepsilon}_{3d_{x^2-y^2}} \end{bmatrix} + \begin{bmatrix} 0 & t_{dd} \\ t_{dd} & 0 \end{bmatrix}, \quad (5c)$$

$$\tilde{\varepsilon}_{\mathbf{k}}^R = \tilde{\varepsilon}_{5d_{z^2}} + t_{RR}(\cos(k_x) + \cos(k_y)), \quad (5d)$$

$$\tilde{\varepsilon}_{\mathbf{k}}^{RNi} = \begin{bmatrix} t'_{dd}s_{k_x}s_{k_y} & t''_{dd}s_{k_x}s_{k_y} \end{bmatrix}, \quad (5e)$$

where

$$s_{k_\nu} = (1 - e^{ik_\nu}) \quad (6)$$

and its complex conjugate $s_{k_\nu}^* = (1 - e^{-ik_\nu})$.

As shown in Figs. 2 and 3, the parameter labeled as t_{pd} represents the hopping between $3d_{x^2-y^2}$ and $2p_{x/y}$ in the $x-y$ plane. t'_{pd} denotes the hopping associated with $3d_{z^2}$ and $2p_{x/y}$. The parameters t'_{dd} and t''_{dd} refer to the hopping involving $5d_{z^2} - 3d_{z^2}$ and $5d_{z^2} - 3d_{x^2-y^2}$, respectively. The t_{dd} describes the hybridization connecting $3d_{z^2}$ and $3d_{x^2-y^2}$ (not shown in Fig. 2). Finally, t_{pp} represents the hopping interaction of $2p_x$ and $2p_y$ in the $x-y$ plane, while t_{RR} corresponds to the hopping within the Rare-earth's $5d_{z^2}$. The overlap values for the RO orbitals are set to zero in the dispersion term based on symmetry considerations, as illustrated in Fig. 3, which indicate cancellation of overlap

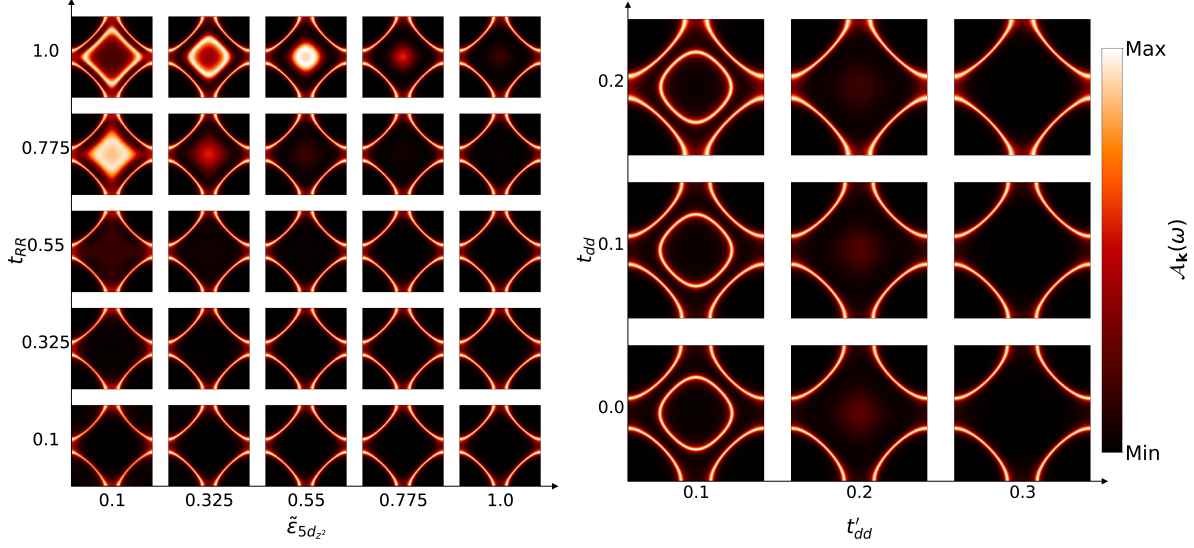


Figure 5: Fermi surface evolution when $\tilde{\epsilon}_{3d_{z^2}} = -0.5 \text{ eV}$ and $\tilde{\epsilon}_{3d_{x^2-y^2}} = -1.0 \text{ eV}$ in $RNiO_2$. Left Panel: Varying t_{RR} and $\tilde{\epsilon}_{5d_{z^2}}$ for a fixed $t'_{dd} = 0.2 \text{ eV}$. Right panel: Varying t'_{dd} and t_{dd} for a fixed $t_{RR} = 0.775 \text{ eV}$ and $\tilde{\epsilon}_{5d_{z^2}} = 0.55 \text{ eV}$. Each Fermi-surface extend from $-\pi$ to π in (k_x, k_y) plane.

for these orbitals (due to bonding and anti-bonding portions of $3d_{x^2-y^2}$ overlapping with the symmetric projection of Rare-earth $5d_{z^2}$). Based on the typical parameters reported from various *ab initio* calculations as listed in Appendix C, common parameters used in the calculation are tabulated in Table. 1. Here, we set an energy difference of

t_{pd}	t_{pp}	t_{dd}	t'_{dd}	t_{RR}	$\tilde{\epsilon}_{3d_{x^2-y^2}} - \tilde{\epsilon}_{2p}$	$\tilde{\epsilon}_{5d_{z^2}}$
1.2 eV	0.6 eV	0.0-0.2 eV	0.1-0.3 eV	0.1-1.0 eV	6 eV	0.1-1.0 eV

Table 1: Summary of common model parameters used (See also Appendix C for a non-exhaustive list of some reported parameters from various *ab-initio* calculations).

6 eV between the $3d_{x^2-y^2}$ and p orbitals, establishing the typical scale for electronic level degeneracy and the positioning of the low-lying Oxygen level. Consequently, the reference $Ni : 3d$ occupancy for $n_{3d_{x^2-y^2}} + n_{3d_{z^2}}$ is approximately 3.2 electrons.

Because of the extended nature of the Rare-earth orbital, the hopping terms t'_{pd} and t''_{dd} are small and thus set to zero. Additionally, the Oxygen $2p$ levels ($\tilde{\epsilon}_{2p}$) lie significantly below the Fermi level $\tilde{\epsilon}_F$. These and other parameter values are provided in Appendix C based on various reported *ab-initio* calculations. Due to the extended nature of the Rare-earth $5d$ orbitals, we explicitly include the direct $R - R$ hopping, denoted as t_{RR} , which can be tuned alongside t'_{dd} and t_{dd} to mimic the effect of reduction of apical Oxygen and compression along the z -axis. At fixed hybridization between $3d_{z^2} - 3d_{x^2-y^2}$ and $3d_{z^2} - 5d_{z^2}$, tuning relative position of Rare-earth $5d_{z^2}$ along with t_{RR} and vice-versa helps to understand the interdependence of the $3d_{z^2}$ orbital and the rare-earth $5d_{z^2}$ orbital. More specifically, to understand the variation in input parameters quantitatively

in layered Nickelates, such as in $PrNiO_2$, we can refer to Table 1 of the reference [42], where there is explicit mention of changes in lattice and hopping parameters with respect to applied pressure. In the extreme case of 150 GPa pressure, the onsite energies and in-plane hopping parameters increase by up to 60%. Pressure along the z -axis results in $\tilde{\epsilon}_{3d_{z^2}} > \tilde{\epsilon}_{3d_{x^2-y^2}}$ below the Fermi level. This conditions tends to reduce the in-plane hopping. Hence Fermi-surface variation with t'_{dd} and t_{dd} is dormant (see Fig.5) while in lowered $\tilde{\epsilon}_{3d_{z^2}} < \tilde{\epsilon}_{3d_{x^2-y^2}}$ condition, the $3d_{z^2}$ acts as a drain for the in-plane conducting electron and contributes as a mediator for super-exchange from $Ni - Ni$ across the layer. It is hence more robust with the change of t'_{dd} and t_{dd} (see Fig.4). A similar trend is also reported in 327 layered Nickelates ($La_3Ni_2O_7$) at 30 GPa [73] where there are evidence of decoupled $3d_{z^2}$ under pressure considering full-band initialization for DFT-based calculation. This model is exemplary in understanding the tunability of the Fermi surface corresponding to the variation in electronic structure due to external pressure or doping. It is to be noted that the emergent secondary pocket in the Fermi surface in this model exists due to interaction between $3d_{z^2}$ and $5d_{z^2}$ while the primary pocket is mainly due to $3d_{x^2-y^2}$. Further, by comparing Fermi-surface variation with variation in $\tilde{\epsilon}_{5d_{z^2}}$ and t_{RR} in Figs. 4, and 5, we can observe that the two-pocket Fermi-surface is more sensitive to the relative difference between $\tilde{\epsilon}_{3d_{x^2-y^2}}$ and $\tilde{\epsilon}_{3d_{z^2}}$ due to the hybridization between $5d_{z^2}$ and $3d_{z^2}$. Consequently, in the case when $\tilde{\epsilon}_{3d_{z^2}} < \tilde{\epsilon}_{3d_{x^2-y^2}}$ the emergence of second Fermi-pocket is more favourable. Hence, this analysis can infer $3d_{z^2}$ as an anchoring orbital level. The relative position of $3d_{z^2}$ to $3d_{x^2-y^2}$ can decide the role of $5d_{z^2}$ in the emergence of an additional Fermi-pocket in the Nickelates system.

2.3. Effective 2-orbital description of $RNiO_2$

In the previous sections, we have shown the anchoring effect of $3d_{z^2}$ and its resemblance to the impact of doping and pressure on the evolution of the Fermi surface. As illustrated in Fig. 7, depending on the change in magnitude of crystal field splitting due to pressure as well as the type of doping (hole or electron), Nickel's $3d_{z^2}$ can either anchor down or up the Rare-earth's $5d_{z^2}$ in terms of energy, leading to the emergence of an additional Fermi pocket.

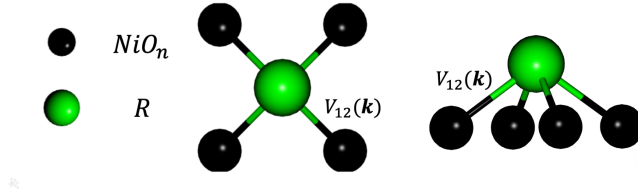


Figure 6: Unit cell of effective $RNiO_2$ system.

One may now ask, what could be an effective model that mimics the Fermi surface's emergent features and trends, as discussed in the section 2.2 for $RNiO_2$? We propose that the adequate multi-orbital description of $RNiO_n$ along with the consideration of

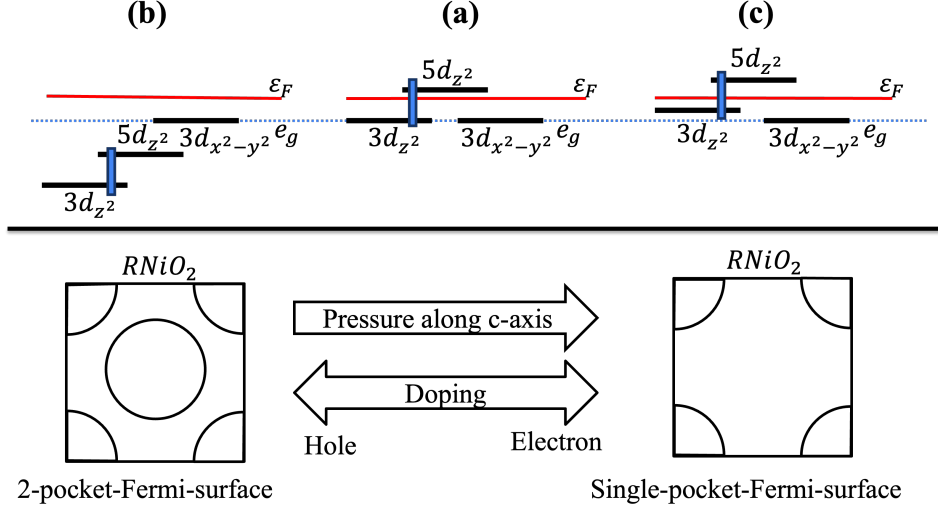


Figure 7: Anchoring effect of $Ni:3d_{z^2}$ with $R:5d_{z^2}$ with condition (a) $\tilde{\epsilon}_{3d_{z^2}} = \tilde{\epsilon}_{3d_{x^2-y^2}}$, (b) $\tilde{\epsilon}_{3d_{z^2}} < \tilde{\epsilon}_{3d_{x^2-y^2}}$, (c) $\tilde{\epsilon}_{3d_{z^2}} > \tilde{\epsilon}_{3d_{x^2-y^2}}$. Mimicking the external doping and applied pressure.

the presence of a second pocket Fermi Surface, can be simplified considering a system consisting of two 2D square lattices (one equivalent to the Rare-Earth layer and another equivalent NiO_n layer with pseudo-orbital equivalent to $3d_{x^2-y^2} + 2p_{x/y}$) as shown in schematic Fig.6.

Theoretically, this sort of reduction can be done using the downfolding method (see Appendix A for more details) of full Hamiltonian Eq. (3) to effective Hamiltonian of form,

$$\mathcal{E}_{eff}(\mathbf{k}) = \begin{bmatrix} \tilde{\mathcal{E}}_1(\mathbf{k}) & V_{12}(\mathbf{k}) \\ V_{12}^*(\mathbf{k}) & \tilde{\mathcal{E}}_2(\mathbf{k}) \end{bmatrix} \quad (7)$$

such that,

$$\tilde{\mathcal{E}}_1(\mathbf{k}) = \tilde{\epsilon}_{\mathbf{k}}^R + \tilde{\epsilon}_{\mathbf{k}}^{RO} [\tilde{\epsilon}_{\mathbf{k}}^O]^{-1} \tilde{\epsilon}_{\mathbf{k}}^{OR}, \quad (8a)$$

$$\tilde{\mathcal{E}}_2(\mathbf{k}) = \tilde{\epsilon}_{\mathbf{k}}^{Ni} + \tilde{\epsilon}_{\mathbf{k}}^{NiO} [\tilde{\epsilon}_{\mathbf{k}}^O]^{-1} \tilde{\epsilon}_{\mathbf{k}}^{ONi}, \quad (8b)$$

$$V_{12}(\mathbf{k}) = \tilde{\epsilon}_{\mathbf{k}}^{RNi} + \tilde{\epsilon}_{\mathbf{k}}^{RO} [\tilde{\epsilon}_{\mathbf{k}}^O]^{-1} \tilde{\epsilon}_{\mathbf{k}}^{ONi}. \quad (8c)$$

This reduction to effective Hamiltonian is restricted to the low-energy description of the system and is allowed only when the energy of ligand (O) is significantly lower than the Fermi level related to other atoms (R, Ni) in the compound. This also assumes that the valence fluctuation on Oxygen can be relatively small, which is the usual case in most layered Nickelates.

For a specific case of $RNiO_2$, we substitute explicit terms from Eq. (5) in Eq. 8 along with the assumptions as mentioned in section 2.2 that due to the influence of

extended Rare-earth orbit, t'_{pd} and t''_{dd} are small and hence are set to zero. Further, as there is no overlap between Rare-earth and Oxygen, hence we can set $\tilde{\epsilon}_{\mathbf{k}}^{RO} = 0$. We thus obtain a generalized form of dispersion as,

$$\tilde{\mathcal{E}}_1(\mathbf{k}) = \tilde{\epsilon}_{5d_{z^2}} + t_{RR} * (\cos(k_x) + \cos(k_y)) \quad , \quad (9)$$

corresponding to Rare-Earth,

$$\tilde{\mathcal{E}}_2(\mathbf{k}) = t_{dd} + \frac{2t_{pd}^2}{\tilde{\epsilon}_{2p}}(\cos(k_x) + \cos(k_y)) \quad , \quad (10)$$

corresponding equivalent NiO_n layer and

$$V_{12}(\mathbf{k}) = t'_{dd} * (1 - e^{k_x}) * (1 - e^{k_y}) \quad (11)$$

is interlayer hybridization.

Therefore, the proposed effective model leads to an effective two-orbital model with dispersion given by equation (7). This model is achieved through an effective two-layer 2D square lattice system with interlayer hybridization $V_{12}(\mathbf{k})$. The key component of this approach is to incorporate the effective in-plane $Ni-O-Ni$ hopping term Eq. (10), which in principle is shared by both families of perovskite and layered Nickelates due to the integration of Oxygen's contribution to the effective NiO_2 layer. Additionally, the formulation explicitly considers the direct $R-R$ hopping term Eq. (9), which is influenced by the presence of a dopant, which can enhance or reduce the interlayer hybridization.

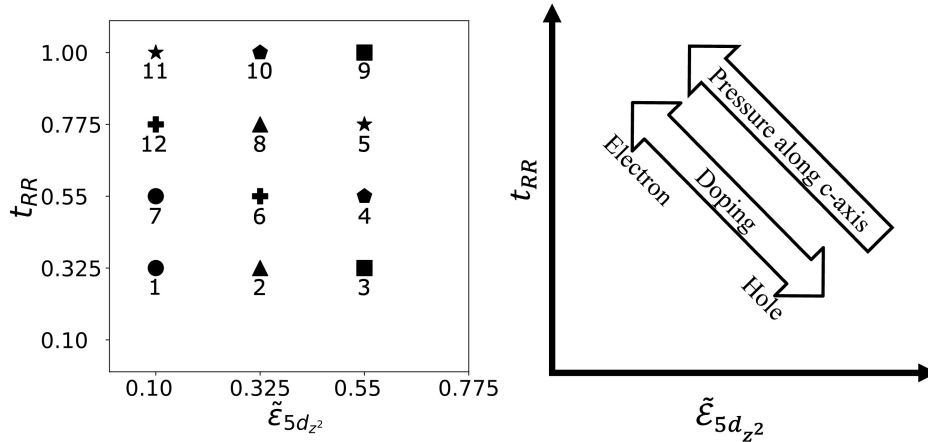


Figure 8: Tuning parameters (Left panel) and schematic of its trend (Right panel) under pressure and doping (see also Table. 2).

To check the equivalence of the effective model, we use a downfolded dispersion matrix Eq. (7) and calculate Fermi-surface evolution using the spectral function from the Green's function formalism Eq. (4) as shown in Fig. 9. We consider three distinct cases for the onsite energies $\tilde{\epsilon}_{3d_{z^2}}$ and $\tilde{\epsilon}_{3d_{x^2-y^2}}$, depicted in Fig. 9: 1.) $\tilde{\epsilon}_{3d_{z^2}} = \tilde{\epsilon}_{3d_{x^2-y^2}}$

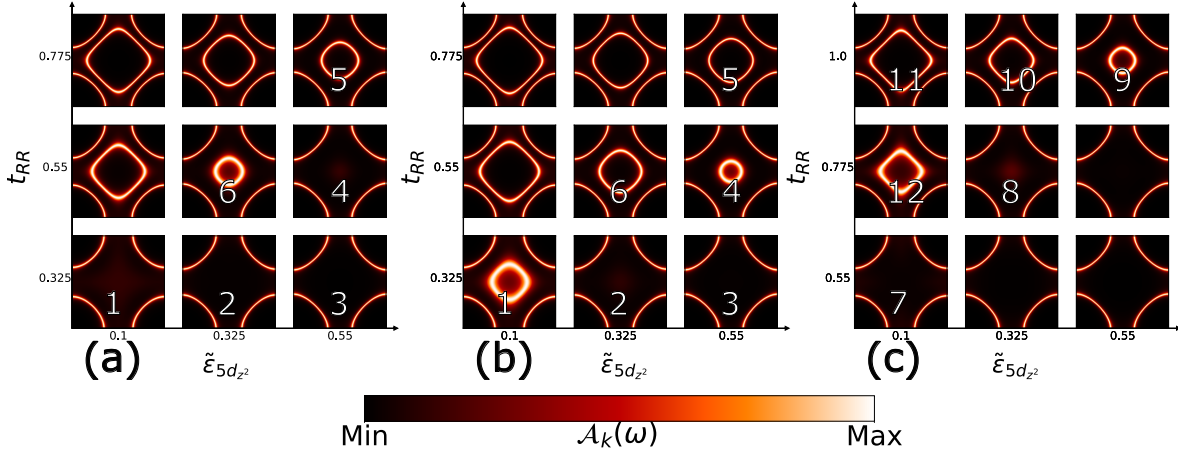


Figure 9: Fermi surface evolution for $RNiO_2$ from our proposed effective model given by dispersion Eq. (7) capturing the similar features of Fermi-surface evolution of multi-orbital model proposed in section (2.2) for $RNiO_2$ with condition (a) $\tilde{\epsilon}_{3d_{z^2}} = \tilde{\epsilon}_{3d_{x^2-y^2}}$, (b) $\tilde{\epsilon}_{3d_{z^2}} < \tilde{\epsilon}_{3d_{x^2-y^2}}$, (c) $\tilde{\epsilon}_{3d_{z^2}} > \tilde{\epsilon}_{3d_{x^2-y^2}}$ mimicking the doping and pressure effect (see Fig. 7). The number in Figures refers to the specific choice of the parameter as mentioned in Fig. 8 (will also be used in section 3 for Lindhard susceptibility calculation see Fig. 11).

(Left panel): This occurs in an undistorted octahedral field environment, and is typically caused by Oxygen ligands, which maintain symmetry and equalizes the $3d$ -orbital energies. 2.) $\tilde{\epsilon}_{3d_{z^2}} < \tilde{\epsilon}_{3d_{x^2-y^2}}$ (Middle panel): square planar field symmetry, lowering the energy of the $3d_{z^2}$ orbital relative to the $3d_{x^2-y^2}$ orbital. 3.) $\tilde{\epsilon}_{3d_{z^2}} > \tilde{\epsilon}_{3d_{x^2-y^2}}$ (Right panel): Under high pressure, orbital overlap increases, raising the energy of $3d_{z^2}$, which leads to an increase in bandwidth and a higher $3d_{z^2}$ energy. These cases mimic the effects of dopants (like Oxygen) and applied pressure (see Fig. 7). Also, using parameters from ref. [74] we calculate the band-structure, density of state, and Fermi-surface as plotted in Fig. 10. By comparison of Fig. 9 with Figs. 4, and 5, we can observe that both multi-orbital model, as well as effective two-orbital models, have a similar emergence of two-pocket Fermi-surface and Fermi-Surface evolution, as discussed in sections (2.2) and (2.2). This can be well understood by this effective two-band model as mentioned in Eq. (7). The layer corresponding to the equivalent square lattice of NiO_2 has the band-contribution from $3d_{x^2-y^2}$ and $2p_{x/y}$ orbitals. The other layer corresponding to the equivalent square lattice of $R - Ni - O$ has band-contribution from $3d_{z^2}$ and $5d_{z^2}$ orbitals, with inter-layer hybridization V_{12} , which can be momentum dependent due to interstitial position of Rare-Earth. We also note that the two Van-Hove singularities (two peaks in the density of states (DOS) in Fig. 10) have the dominant contribution of $R - Ni$ and $Ni - O$ orbitals. While tuning the parameters in these systems, the Fermi surface changes. The appearance of a secondary Fermi pocket is realized when the Van-hove singularity of $R - Ni$ moves much closer to the Van-hove singularity of $Ni - O$. Indeed, the downfolding method will lose the occupancy count of the band

under the scrutiny of empirical evidence of input parameters and full-band Density Functional Theory (*ab-initio*) analysis. However, it will preserve a consistent trend of inter-dependence of parameters and the order of magnitude and effectively gives the emergence and evolution of a two-pocket-Fermi surface

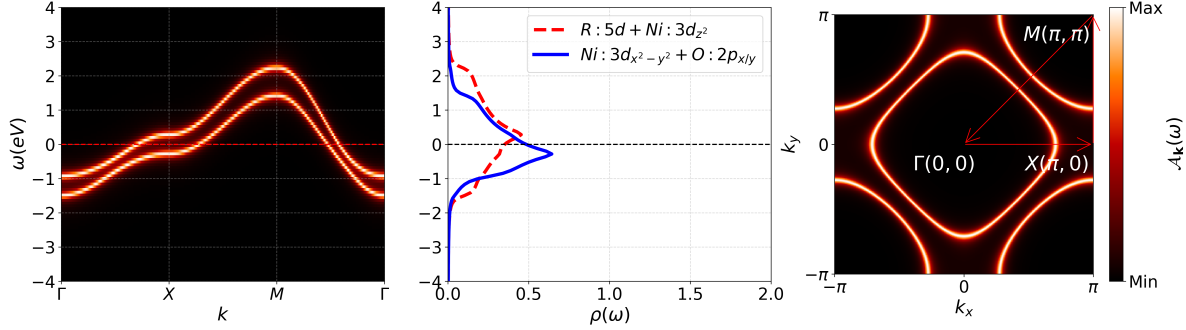


Figure 10: Bands Structure, Orbital-Resolved Density of States and Fermi-Surface from effective 2-orbital description with dispersion given by Eq. (7) using parameters from ref. [74]

Thus, we have examined a generalized phenomenological model based on an understanding of the relevant multi-orbital model, which consists of Nickel $3d_{z^2}$ and Rare-earth $5d_{z^2}$ in layered Nickelates (see Fig. 7). This has led to an effective two-orbital model for $RNiO_2$. Our phenomenological understanding emphasizes the role of $3d_{z^2}$ as an anchoring energy level, which in our model can be explicitly captured in the interlayer hybridization term $V_{12}(\mathbf{k})$ (see Fig. 6) in dispersion equation (7). This effective model retains the Fermi-surface evolution features of the multi-orbital model, even with the qualitative tuning of doping and pressure. Therefore, it can be utilized to calculate other physical observables. For example, in the subsequent section (3), we use it to calculate the static susceptibility in the considered system, helping us understand the nature of electronic excitation and instabilities.

3. Spin and Charge susceptibilities

In this section, we analyze the spin and charge channels of instabilities by evaluating the Lindhard susceptibility within the framework of our effective two-orbital model Eq. (7). We aim to determine how well this two-orbital model captures the key physical phenomena, such as spin and charge instabilities relevant to high- T_c superconductivity [75]. These instabilities often emerge from the complex interplay between charge, spin, and orbital degrees of freedom. They can lead to transitions in the pairing symmetry and gap structure of the superconducting state. In particular, spin and charge fluctuations may drive the system towards different ordered phases, such as charge-density waves, spin-density waves, or superconducting phases. Observables like susceptibility can provide valuable insights into these instabilities by probing the behavior in charge or spin channels.

We define, multiorbital site-dependant charge susceptibility as,

$$\chi_{ij}^{AB}(\tau)|_c \equiv -\langle n_i^A(\tau) n_j^A(0) \rangle \quad (12)$$

such that, Operator $n_i^A = c_i^{\dagger A\uparrow} c_i^{A\uparrow} + c_i^{\dagger A\downarrow} c_i^{A\downarrow} - n$ where n is the average number of occupancy. Similarly, we define spin susceptibility as,

$$\chi_{ij}^{AB}(\tau)|_s \equiv -\langle \mathcal{S}_i^{A,+}(\tau) \mathcal{S}_j^{B,-}(0) \rangle \quad (13)$$

where, $\mathcal{S}_i^{A,+} = c_i^{\dagger A\uparrow} c_i^{A\downarrow}$, $\mathcal{S}_i^{A,-} = c_i^{\dagger A\downarrow} c_i^{A\uparrow}$. In a non-interacting system with a paramagnetic state, we can apply Wick's Theorem and express the charge Eq. (12) and spin susceptibility Eq. (13) in terms of the product of two single-particle Green's function such that (see Appendix B)

$$\chi_{ij}^{AB}(\tau)|_s = \frac{1}{2} \chi_{ij}^{AB}(\tau)|_c = \chi_{0ij}^{AB}(\tau) \equiv -\mathcal{G}_{ij}(\tau) \mathcal{G}_{ji}(-\tau) \quad (14)$$

where χ_{0ij}^{AB} is defined as Lindhard susceptibility. Fourier transform of Lindhard susceptibility is given by,

$$\chi_0^{AB}(\mathbf{q}, \omega) = -\frac{1}{\beta} \sum_{\mathbf{k}} \sum_{\omega_n} \mathcal{G}^{A-B}(\mathbf{k}, i\omega_n) \mathcal{G}^{B-A}(\mathbf{k} + \mathbf{q}, i\omega_n + \omega) \quad (15)$$

where $i\omega_n$ is Matsubara frequency, ω is the bosonic frequency, β is the inverse temperature, and $\mathcal{G}^{A-B}(\mathbf{k}, i\omega_n)$ is the single-particle Green's function for orbital indices A and B. This is, in principle, a response of material to an external field, the peak of which also gives the optimal direction of momentum-dependent fluctuation/instabilities or potential ordering.

Similar to previous section 2.3 we computed Lindhard susceptibility $\chi_0(\mathbf{q}, \omega = 0)$ for three different condition Fig. 11(a) $\tilde{\epsilon}_{3d_{z^2}} = \tilde{\epsilon}_{3d_{x^2-y^2}}$, Fig. 11(b) $\tilde{\epsilon}_{3d_{z^2}} < \tilde{\epsilon}_{3d_{x^2-y^2}}$ and Fig. 11(c) $\tilde{\epsilon}_{3d_{z^2}} > \tilde{\epsilon}_{3d_{x^2-y^2}}$. Again these three condition mimic the effects of dopants(like Oxygen) and applied pressure as depicted in Figure. 7. Using the proposed effective model given by the dispersion equation (7) for each of these cases, we tune the parameters depicted by labels 1 – 12 shown Table 2(or Fig.8). These parameters are intentionally selected to take into account all possible variations of the tunable parameter to check its effect on $\chi_0(\mathbf{q}, \omega = 0)$ with the emergence of secondary Fermi-pocket. To understand the trend, consider the plotted $\chi_0(\mathbf{q}, \omega = 0)$ in Fig.11 for different parameters with labels as mentioned in Table 2. When $\tilde{\epsilon}_{5d_{z^2}}$ varies with a constant t_{RR} , χ_0^R sequentially decreases with an increasing $\tilde{\epsilon}_{5d_{z^2}}$. This trend of χ_0^R is similar for all three conditions $\tilde{\epsilon}_{3d_{z^2}} = \tilde{\epsilon}_{3d_{x^2-y^2}}$, $\tilde{\epsilon}_{3d_{z^2}} < \tilde{\epsilon}_{3d_{x^2-y^2}}$, and $\tilde{\epsilon}_{3d_{z^2}} > \tilde{\epsilon}_{3d_{x^2-y^2}}$. When t_{RR} varies with a constant $\tilde{\epsilon}_{5d_{z^2}}$, χ_0^R sequentially increases with an increasing t_{RR} . This trend of χ_0^R is also similar for all three cases mentioned earlier. Finally, when both $\tilde{\epsilon}_{5d_{z^2}}$ vary with t_{RR} , χ_0^R sequentially increases with a decreasing $\tilde{\epsilon}_{5d_{z^2}}$ and t_{RR} . This χ_0^R trend is consistent over all three cases. It is evident from plotted Fig. 11 that this trend of χ_0^R becomes more dormant when $\tilde{\epsilon}_{3d_{z^2}} < \tilde{\epsilon}_{3d_{x^2-y^2}}$. Further, χ_0^{Ni-R} is consistently near 0

throughout all the cases. χ_0^{Ni} follows the same trend as χ_0^R but is less robust compared to χ_0^R and shows a consistent peak at $\mathbf{q}_0 = (\pi, \pi)$, which has been explicitly observed through reported *ab-initio* calculations [76, 77, 78] and a small crest at $\mathbf{q}_0 = (\pi, 0)$ throughout all the cases. For the variation of $\tilde{\epsilon}_{5d_{z^2}} - t_{RR}$, χ_0^R shows a consistent peak at $\mathbf{q}_0 = (0, 0)$.

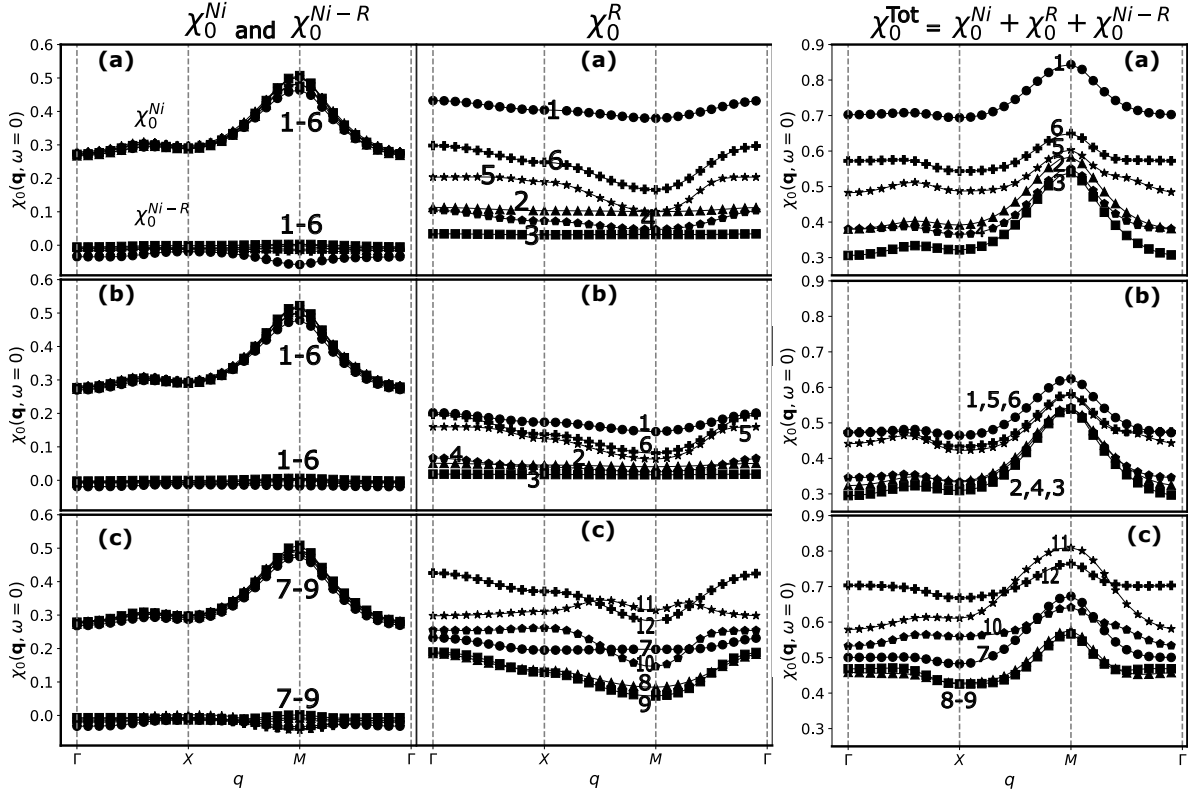


Figure 11: Lindhard susceptibility components of $RNiO_2$ with condition (a) $\tilde{\epsilon}_{3d_{z^2}} = \tilde{\epsilon}_{3d_{x^2-y^2}}$, (b) $\tilde{\epsilon}_{3d_{z^2}} < \tilde{\epsilon}_{3d_{x^2-y^2}}$, (c) $\tilde{\epsilon}_{3d_{z^2}} > \tilde{\epsilon}_{3d_{x^2-y^2}}$ (see Fig. 7) following parameters with labels mentioned in Table 2 (see also Fig. 8) from our proposed effective model Eq. (7). Left panels χ_0^{Ni} and χ_0^{Ni-R} , Center panels χ_0^R and Right panels $\chi_0^{Tot} = \chi_0^{Ni} + \chi_0^R + \chi_0^{Ni-R}$.

Instabilities in the spin or charge channels can be understood by interacting susceptibilities, $\chi(\mathbf{q}, \omega)|_s = \chi_0(\mathbf{q}, \omega)/(1 + V(\mathbf{q})_s \chi_0(\mathbf{q}, \omega))$ for spin and $\chi(\mathbf{q}, \omega)|_c = \chi_0(\mathbf{q}, \omega)/(1 - V(\mathbf{q})_c \chi_0(\mathbf{q}, \omega))$ for charge in RPA formalism. Where $\chi_0(\mathbf{q}, \omega)$ is the Lindhard susceptibility and $V(\mathbf{q})_s$ and $V(\mathbf{q})_c$ are the effective interaction strength. In the spin channel, a divergence in $\chi(\mathbf{q}, \omega)$ suggests instabilities towards magnetic ordering, such as the formation of spin density wave (SDWs) and $V(\mathbf{q})_s$ corresponds to effective spin-spin interaction such as Heisenberg or Hund type exchange interaction and the peak in $\chi(\mathbf{q}, \omega)$ corresponds to the nesting wave vector where SDW formation is energetically favourable. In the charge channel, divergence indicates a tendency towards charge ordering, such as the formation of charge-density waves (CDWs). Peaks in χ_0 correspond to wave vectors favouring SDW or CDW formation. In the charge channel, the $V(\mathbf{q})_c$ corresponds to effective charge-charge interaction such as Coulomb

$\tilde{\epsilon}_{5d_{z^2}} \backslash t_{RR}$	0.10	0.325	0.55
1.00	11	10	9
0.775	12	8	5
0.55	7	6	4
0.325	1	2	3

Table 2: Table of parameters followed for calculating $\chi_0(\mathbf{q}, 0)$ in Fig. 11 for $RNiO_2$ from proposed effective model given by dispersion Eq. (7). All values are in eV

exchange interaction and the peak in $\chi(\mathbf{q}, \omega)$ corresponds to the nesting wave vector where electronic density exhibits a modulation in the direction of specific wave-vector. Thus, the RPA takes into account how interactions affect the Lindhard susceptibility, resulting in an increased response at specific wave vectors (\mathbf{q}_0) and frequencies (ω) where collective excitations or instabilities may occur. When the Lindhard susceptibility is sufficiently large ($\chi_0(\mathbf{q}, \omega) \sim V(\mathbf{q})_s^{-1}$ or $V(\mathbf{q})_c^{-1}$), the system becomes prone to long-range ordering. In our model, considering the spin channel, an increase in interlayer hybridization is observed when $\tilde{\epsilon}_{3d_{z^2}} < \tilde{\epsilon}_{3d_{x^2-y^2}}$. In this scenario, we observe a dominant contribution of χ_0^{Ni} near $\mathbf{q}_0 = (\pi, \pi)$ (the M -point) compared to a relatively inactive χ_0^R in χ_0^{Tot} . This suggests the emergence of an antiferromagnetic-ordered state, similar to Cuprates [79, 80, 81, 82, 83, 84, 85, 86]. In Cuprates, doping rapidly disrupts this long-range order, indicating the emergence of short-range magnetic correlations due to magnetic instabilities. This shift in magnetic behaviour underscores the potential role of spin fluctuations in the electronic pairing mechanisms [87]. A similar emergence has been reported in determinant quantum Monte Carlo (DQMC) studies in Layered Nickelates. Furthermore, in layered Nickelates, the reduction in the dimensionality of the magnetic fluctuations (from 3D to 2D) coincides with the emergence of superconductivity, which aligns with our assumptions and results for the proposed effective model. However, on the other hand, χ_0^R shows an emergence of a peak at $\mathbf{q}_0 = (0, 0)$ (the Γ -point) when the energy of the $\tilde{\epsilon}_{3d_{z^2}}$ orbital exceeds or equals that of the $\tilde{\epsilon}_{3d_{x^2-y^2}}$ orbital. This suggests the emergence of ferromagnetic ordering, which is highly unlikely to be the origin of the emergence of any superconducting order. It is noted that there are several theoretical and experimental attempts to investigate the pairing mechanism [88, 39, 89] in $R_3Ni_2O_7$ and elevating the T_c in $Pr_{1-x}Sr_xNiO_2$ [90, 42].

The peak in χ_0^{Tot} is generally attributed to ordering tendency or instabilities-whether spin or charge. These peaks are typically associated with Fermi surface nesting or other mechanisms that enhance the electronic response at specific wave vectors. In our model for layered Nickelates, increasing pressure enhances the ordering

tendency and favors the formation of a single-pocket Fermi surface, consistent with recent experimental results [42]. Similarly, optimal doping—whether electron or hole doping—also strengthens the overall tendency for ordering and the appearance of a single-pocket Fermi surface, as confirmed by recent ARPES measurements [16, 17, 43]. Our case of $\tilde{\epsilon}_{3d_{z^2}} = \tilde{\epsilon}_{3d_{x^2-y^2}}$ corresponds to electron doping which can induce a phase transition to a structurally ordered state. For example, excess oxygen doping in layered Nickelates may result in a transition to a complete perovskite phase, which would explain the observation of a two-pocket Fermi surface resembling that of perovskite phases [91, 92]. The complementary explanations could be that the incomplete reduction can lead to residual ordering as observed in $Ni - L_3$ edge resonant X-ray scattering experiment [8], whereas complete reduction to the layered phase shows no evidence of any ordered phase[9].

Thus, from our proposed model, we computed the Lindhard susceptibility $\chi_0(\mathbf{q}, 0)$ for various energy configurations to simulate the effects of doping and applied external pressure qualitatively. Doping and applied external pressure can be attributed to the competition between different ordering wave vectors originating from Rare-earth and Nickel. Similar to CuO_2 layer in Cuprates superconductors, NiO_2 also has tendency of $\mathbf{q}_0 = (\pi, \pi)$ ordering. However, depending on external factors such as doping or pressure, Rare-earth might compensate for this order. We also discussed the versatility of our model to aid the understanding of electronic charge or spin instabilities in layered Nickelates.

4. Conclusion

This study provides a comprehensive modelling framework for understanding the role of effective orbitals and the emergence of an additional Fermi pocket in layered Nickelates. The analysis shows that the Nickel $3d_{x^2-y^2}$ orbital mainly crosses the Fermi level, while the Nickel $3d_{z^2}$ orbital acts as an anchor to lowering the energy of the Rare-earth $5d_{z^2}$ orbital, leading to the emergence of a second Fermi surface pocket. This anchoring effect of $3d_{z^2}$ allows an effective two-orbital description involving both Nickel and Rare-earth, explaining how the Fermi surface emergence evolves with doping and pressure qualitatively-similar to features seen in Cuprate superconductors.

Based on our observations in Lindhard susceptibility calculations, we cannot confirm any instabilities at $\mathbf{q}_0 = (\frac{1}{3}, 0)$ in reciprocal lattice units (r.l.u), as suggested by resonant X-ray scattering experiment [8]. However, our findings on susceptibility indicate potential instabilities at $\mathbf{q}_0 = (\pi, \pi)$ (or $\mathbf{q}_0 = (\frac{1}{2}, \frac{1}{2})$ in r.l.u), similar to those observed in Cuprates. The peak in Lindhard susceptibility could be attributed to the strong influence of the underlying square lattice symmetry, similar to Cuprates and is tunable with pressure and doping. Specific interaction terms must be considered to understand the microscopic pairing mechanism for superconductivity, whether it involves CDW, charge order, or magnetic order. This sheds light on the most relevant interaction and provides insights into the microscopic pairing mechanism for

superconductivity. The observed Lindhard susceptibility peak at $\mathbf{q}_0 = (\pi, \pi)$ will be crucial for the emergence of any ordering instability, including superconductivity, resulting from microscopic interaction terms. The proposed modelling framework provides a comprehensive approach to studying the effects of doping and pressure in the Nickelate family. It offers insights into the factors influencing susceptibilities, such as Fermi-surface nesting, which significantly impact the fluctuation spectrum.

The proposed two-orbital effective model for layered Nickelates could be used in further work incorporating electronic interactions more accurately, which will provide deeper insights into phenomena such as charge and spin density waves, ordering, and other instabilities contributing to superconductivity. Further investigation of varying doping levels and external pressures, informed by empirical data and *ab initio* calculations, is also recommended. Experimental studies of (π, π) instabilities in the spin sector, such as spin-density waves and Néel order, and in the charge sector, like charge-density waves, could offer crucial evidence. If the origin and presence or absence of correlations are confirmed experimentally, they would significantly enhance our understanding of the emergence of superconductivity in Nickelates and their connection to Cuprates.

ACKNOWLEDGMENTS

This work has been supported by Centre national de la recherche scientifique (CNRS) and Agence National de Recherche (ANR) grant SuperNickel (ANR-21-CE30-0041-02)

Supplementary Material: Emergence and tunability of Fermi-pocket and electronic instabilities in layered Nickelates

Effect of Three dimensionality

Three-dimensionality plays a crucial role in understanding perovskite Nickelates' electronic and structural properties. These materials exhibit rich phase diagrams and intriguing phenomena such as metal-insulator transitions and high-temperature superconductivity. The three-dimensional nature of the crystal structure and electronic interactions introduces complexity, especially when considering the interactions between atoms along different crystallographic axes. However, in many cases, this complexity can be effectively captured by approximations that simplify the problem. One such approach is to fix the k_z momentum component, assuming only the on-site energy is renormalized. This simplification reduces the computational burden while preserving essential features of the system's three-dimensional behavior. It allows for a more tractable analysis of their electronic properties without sacrificing key physical insights.

Recent progress in superconductivity studies of layered Nickelates such as $RNiO_2$ has highlighted the importance of these three-dimensional considerations for consistently synthesizing the parent perovskite compound $RNiO_3$ and its subsequent reduction to $RNiO_2$ [5]. The transformation from perovskite $RNiO_3$ to the superconducting $RNiO_2$ phase, such as $LaNiO_2$, $NdNiO_2$, and $PrNiO_2$, involves the selective removal of apical Oxygen, which alters the electronic structure and dimensionality. These layered Nickelates exhibit superconductivity when hole-doped, typically by substituting rare-earth elements with Sr or Ca [1, 2, 3, 4, 5, 6].

In perovskite Nickelates, the Fermi surface is predominantly shaped by the $3d_{x^2-y^2}$ and $3d_{z^2}$ orbitals of Nickel, with electron hopping occurring through two primary mechanisms: an in-plane channel involving the $3d_{x^2-y^2}$ orbital hybridizing with Oxygen $2p_x$ and $2p_y$, and an out-of-plane channel where the $3d_{z^2}$ orbital hybridizes with apical Oxygen $2p_z$ [40]. Additional contributions from rare-earth $5d_{z^2}$ orbitals further complicate the three-dimensional electronic structure, which must be accounted for when constructing a generalized Hamiltonian.

This generalized Hamiltonian incorporates key orbitals—rare-earth $5d_{z^2}$, Nickel $3d_{x^2-y^2}$ and $3d_{z^2}$, and Oxygen $2p_{x/y/z}$ —and models electron hopping through neighboring Oxygen p -states as a virtual process. The block-diagonal form of the Hamiltonian reflects the non-degenerate on-site energies of the transition metal and rare-earth orbitals, while the degenerate, lower-energy Oxygen p -orbitals preserve key symmetries. By fixing the k_z component and focusing on on-site energy renormalization, the dimensional reduction captures essential three-dimensional effects, enabling a unified description of both perovskite $RNiO_3$ and superconducting $RNiO_2$, without losing the characteristic emergence of the two-pocket Fermi surface.

Thus, the blocks in Eq. (3) are given by,

$$\tilde{\varepsilon}_{\mathbf{k}}^O = \tilde{\varepsilon}_{2p} + \begin{bmatrix} 0 & t_{pp}s_{k_x}s_{k_y}^* \\ t_{pp}s_{k_x}^*s_{k_y} & 0 \end{bmatrix} + \begin{bmatrix} 0 & t_{pp}^\perp s_{k_z} \\ t_{pp}^\perp s_{k_z}^* & 0 \end{bmatrix} \quad (16a)$$

$$\tilde{\varepsilon}_{\mathbf{k}}^{NiO} = \begin{bmatrix} -t'_{pd}s_{k_x} & -t'_{pd}s_{k_y} \\ t_{pd}s_{k_x} & -t_{pd}s_{k_y} \end{bmatrix} + \begin{bmatrix} 0 & t_{pd}^\perp s_{k_z} \\ 0 & 0 \end{bmatrix} \quad (16b)$$

$$\tilde{\varepsilon}_{\mathbf{k}}^{Ni} = \begin{bmatrix} \tilde{\varepsilon}_{3d_{z^2}} & 0 \\ 0 & \tilde{\varepsilon}_{3d_{x^2-y^2}} \end{bmatrix} + \begin{bmatrix} 0 & t_{dd} \\ t_{dd} & 0 \end{bmatrix} + \begin{bmatrix} 0 & t_{dd}^\perp s_{k_z} \\ t_{dd}^\perp s_{k_z}^* & 0 \end{bmatrix} \quad (16c)$$

$$\tilde{\varepsilon}_{\mathbf{k}}^R = \tilde{\varepsilon}_{5d_{z^2}} + t_{RR}(\cos(k_x) + \cos(k_y)) + t_{RR}^\perp \cos(k_z) \quad (16d)$$

$$\tilde{\varepsilon}_{\mathbf{k}}^{RNi} = \begin{bmatrix} t'_{dd}s_{k_x}s_{k_y} & t''_{dd}s_{k_x}s_{k_y} \\ t'_{dd}s_{k_z} & 0 \end{bmatrix} + \begin{bmatrix} t'_{dd}^\perp s_{k_z} & 0 \\ 0 & 0 \end{bmatrix} \quad (16e)$$

where

$$s_{k_\nu} = (1 - e^{ik_\nu}) \quad (17)$$

and its complex conjugate $s_{k_\nu}^* = (1 - e^{-ik_\nu})$.

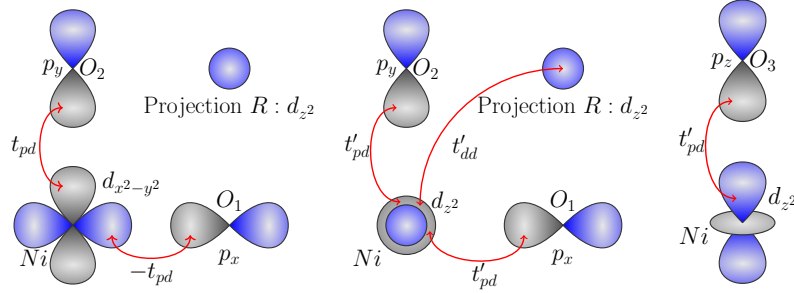


Figure 12: Orbital overlaps and the hopping parameter considering the orbital symmetry of $RNiO_n$ and the in-plane Oxygen atoms O_1 and O_2 as well as the out-of-plane Oxygen atom O_3 .

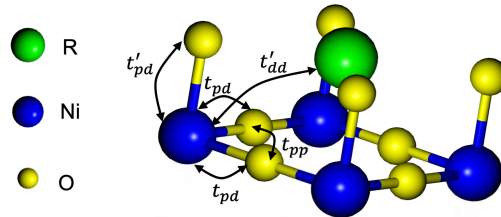


Figure 13: Schematic of in-plane and out-plane hopping parameter in $RNiO_3$.

As shown in Figs. 13 and 12, the parameter labeled as t_{pd} represents the hopping parameter between $3d_{x^2-y^2} - 2p_{x/y}$ in the $x-y$ plane. t'_{pd} denotes the hopping parameter

between the $3d_{z^2} - 2p_z$ out of the $x - y$ plane. The parameters t'_{dd} , t''_{dd} correspond to the hopping parameters between $5d_{z^2} - 3d_{z^2}$ and $5d_{z^2} - 3d_{x^2-y^2}$ respectively. The t_{dd} represents the hybridization between $3d_{z^2} - 3d_{x^2-y^2}$. Finally, t_{pp} denotes the hopping parameter between $2p_x - 2p_y$ in the $x - y$ plane, and t_{RR} is the hopping between the Rare-earth's $5d_{z^2}$. Further, the parameters t_{pp}^\perp , t_{pd}^\perp and t_{dd}^\perp corresponds to out of plane (perpendicular) component of $2p_{x/y} - 2p_z$, $3d_{z^2} - 3p_z$ and $5d_{z^2} - 3d_{z^2}$ hopping respectively and t_{dd}^\perp , t_{RR}^\perp is out of plane (perpendicular) component of hybridization between $Ni - Ni$ and $R - R$ orbitals. At a fixed value of k_z , these t^\perp 's renormalize the on-site contribution of the corresponding orbital. In our calculation, we fix this $k_z = 0$ and assume the same fixed parameter as of layered Nickelates except for the degeneracy of e_g . Indeed, this is over-simplification, but the aim here is explicitly limited to proposing the model for perovskite structure in the spirit, of same assumption as for layered structure.

Further, in perovskite $RNiO_3$ compounds, the octahedral crystal field induces a level splitting such that $t_{2g} < e_g$, leaving the $3d_{z^2}$ and $3d_{x^2-y^2}$ orbitals degenerate. Our model accounts for the symmetry constraints that prevent orbital overlap between the $5d_{z^2}$ and $2p_{x/y/z}$ orbitals, as well as between the $2p_z$ and in-plane $2p_{x/y}$ and $3d_{x^2-y^2}$ orbitals. To examine the effect of apical Oxygen on orbital energies within our multi-orbital model of $RNiO_3$, described by the dispersion in Eq. (16), we analyze the interplay among the $5d_{z^2}$, $3d_{x^2-y^2}$, $3d_{z^2}$, and $2p_x$, $2p_y$, $2p_z$ orbitals. By adjusting the relative energy scales and hopping parameters, we aim to tune the model to capture the critical emergence of an additional Fermi pocket using a spectral function Eq. (4) derived from Green's function formalism. This parametrization tuning results in a Fermi surface that spans the Brillouin zone from antinodal to nodal regions. Notably, there is a varying energy gap along the antinodal direction compared to the nodal direction, reflecting a substantial pocket centered at $\Gamma(0,0)$, extending from $-\pi$ to π in the high-symmetry plane $\Gamma(0,0) - X(\pi,0) - M(\pi,\pi) - \Gamma(0,0)$, as shown in Fig. 14.

Thus, the Fermi surface evolution depicted in Fig. 14 explores the versatility of our 6-band model's behavior, with dispersion given by Eq. (16). By varying different parameters, it elucidates the interdependence of the $3d_{z^2}$ and Rare-earth $5d_{z^2}$ orbitals and the resulting formation of one or two Fermi surface pockets. As we have considered degenerate e_g near the Fermi level, one may expect the direct contribution of these levels on the Fermi surface. However, as aforementioned due to symmetry reasons $3d_{z^2}$ rather overlap significantly with $5d_{z^2}$ causing extended orbitals. Hopping through these extended orbitals results in the second pocket in the Fermi surface. This pocket is robust over variation of hopping amplitude between $5d_{z^2} - 3d_{z^2}$ but dormant with variation in hopping amplitude between $3d_{z^2} - 3d_{x^2-y^2}$. Thus, we can safely include the $3d_{z^2}$ as the anchoring orbital for proposing the two orbital effective model, discussed in detail in section 2.3 in main text.

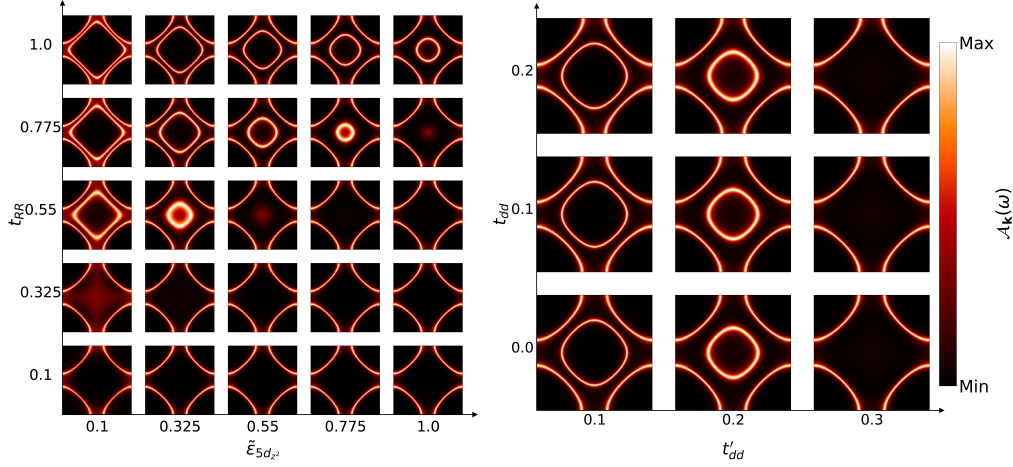


Figure 14: Fermi surface evolution in $RNiO_3$. Left Panel: Varying t_{RR} and $\tilde{\epsilon}_{5d_{z^2}}$ for a fixed $t'_{dd} = 0.2 \text{ eV}$ and $\tilde{\epsilon}_{3d_{z^2}} = \tilde{\epsilon}_{3d_{x^2-y^2}} = -1.0 \text{ eV}$. Right panel: Varying t'_{dd} and t_{dd} for a fixed $t_{RR} = 0.775 \text{ eV}$ and $\tilde{\epsilon}_{5d_{z^2}} = 0.55 \text{ eV}$, with $\tilde{\epsilon}_{3d_{z^2}} = \tilde{\epsilon}_{3d_{x^2-y^2}} = -1.0 \text{ eV}$. Each Fermi-surface extend from $-\pi$ to π in (k_x, k_y) plane.

Appendix A. Downfolding

This method of reduction is permitted because of low-lying Oxygen. In principle, we can safely downfold (integrate out) Oxygen's contribution to the dispersion, yielding an effective Hamiltonian. This new downfolded Hamiltonian is restricted to the low-energy description. For full Hamiltonian of form of Eq.(2) the Green's function matrix have form of,

$$\mathcal{G}_{\mathbf{k}}(\omega) = \begin{bmatrix} \mathcal{G}_{\mathbf{k}}^R(\omega) & \mathcal{G}_{\mathbf{k}}^{RNi}(\omega) & \mathcal{G}_{\mathbf{k}}^{RO}(\omega) \\ \mathcal{G}_{\mathbf{k}}^{NiR}(\omega) & \mathcal{G}_{\mathbf{k}}^{Ni}(\omega) & \mathcal{G}_{\mathbf{k}}^{NiO}(\omega) \\ \mathcal{G}_{\mathbf{k}}^{OR}(\omega) & \mathcal{G}_{\mathbf{k}}^{ONi}(\omega) & \mathcal{G}_{\mathbf{k}}^O(\omega) \end{bmatrix} \quad (\text{A.1})$$

with dimension $N \times N$. Where, each element $\mathcal{G}_{\mathbf{k}}(\omega) = (\omega - \tilde{\epsilon}_{\mathbf{k}})^{-1}$. Upon downfolding Oxygen contribution, we can have the effective Green's function matrix of size $(N - N_O) \times (N - N_O)$ such that,

$$\mathcal{G}_{eff}(\mathbf{k}, \omega) = \begin{bmatrix} \mathcal{G}_{\mathbf{k}}^R(\omega) & \mathcal{G}_{\mathbf{k}}^{RNi}(\omega) \\ \mathcal{G}_{\mathbf{k}}^{NiR}(\omega) & \mathcal{G}_{\mathbf{k}}^{Ni}(\omega) \end{bmatrix} \quad (\text{A.2})$$

where we introduce self energy contribution $\Sigma(\mathbf{k}, \omega)$ such that,

$$\begin{aligned}
\left[\mathcal{G}_{eff}(\mathbf{k}, \omega) \right]^{-1} &= \omega \mathbb{1} - \left[\begin{array}{c|c} \tilde{\varepsilon}_{\mathbf{k}}^R & \tilde{\varepsilon}_{\mathbf{k}}^{RNi} \\ \hline \tilde{\varepsilon}_{\mathbf{k}}^{NiR} & \tilde{\varepsilon}_{\mathbf{k}}^{Ni} \end{array} \right] + \left[\begin{array}{c|c} \Sigma_{\mathbf{k}}^R(\omega) & \Sigma_{\mathbf{k}}^{RNi}(\omega) \\ \hline \Sigma_{\mathbf{k}}^{NiR}(\omega) & \Sigma_{\mathbf{k}}^{Ni}(\omega) \end{array} \right] \\
&= (\omega \mathbb{1} - \mathcal{E}_{eff}(\mathbf{k}, \omega)) \approx (\omega \mathbb{1} - \mathcal{E}_{eff}(\mathbf{k}))
\end{aligned} \tag{A.3}$$

such that,

$$\Sigma_{\mathbf{k}}^R(\omega) = \tilde{\varepsilon}_{\mathbf{k}}^{RO} [\omega - \tilde{\varepsilon}_{\mathbf{k}}^O]^{-1} \tilde{\varepsilon}_{\mathbf{k}}^{OR} \tag{A.4a}$$

$$\Sigma_{\mathbf{k}}^{Ni}(\omega) = \tilde{\varepsilon}_{\mathbf{k}}^{NiO} [\omega - \tilde{\varepsilon}_{\mathbf{k}}^O]^{-1} \tilde{\varepsilon}_{\mathbf{k}}^{ONi} \tag{A.4b}$$

$$\Sigma_{\mathbf{k}}^{RNi}(\omega) = \tilde{\varepsilon}_{\mathbf{k}}^{RO} [\omega - \tilde{\varepsilon}_{\mathbf{k}}^O]^{-1} \tilde{\varepsilon}_{\mathbf{k}}^{ONi} \tag{A.4c}$$

On the general ground, this method of downfolding is exact since we do not consider interaction in our model for the Oxygen orbitals. The self energies are ω -dependent, however we assume that the energies of $\tilde{\varepsilon}_{\mathbf{k}}^O$ are far from the Fermi-level of R and Ni electrons. Therefore, we can neglect this ω dependence and approximate these self-energies by their static ($\omega = 0$) components. Thus, from effective Green's function Eq. (A.2) we can have effective dispersion of form,

$$\mathcal{E}_{eff}(\mathbf{k}) = \left[\begin{array}{c|c} \tilde{\mathcal{E}}_1(\mathbf{k}) & V_{12}(\mathbf{k}) \\ \hline V_{12}^*(\mathbf{k}) & \tilde{\mathcal{E}}_2(\mathbf{k}) \end{array} \right] \tag{A.5}$$

such that,

$$\tilde{\mathcal{E}}_1(\mathbf{k}) = \tilde{\varepsilon}_{\mathbf{k}}^R + \tilde{\varepsilon}_{\mathbf{k}}^{RO} [\tilde{\varepsilon}_{\mathbf{k}}^O]^{-1} \tilde{\varepsilon}_{\mathbf{k}}^{OR} \tag{A.6a}$$

$$\tilde{\mathcal{E}}_2(\mathbf{k}) = \tilde{\varepsilon}_{\mathbf{k}}^{Ni} + \tilde{\varepsilon}_{\mathbf{k}}^{NiO} [\tilde{\varepsilon}_{\mathbf{k}}^O]^{-1} \tilde{\varepsilon}_{\mathbf{k}}^{ONi} \tag{A.6b}$$

$$V_{12}(\mathbf{k}) = \tilde{\varepsilon}_{\mathbf{k}}^{RNi} + \tilde{\varepsilon}_{\mathbf{k}}^{RO} [\tilde{\varepsilon}_{\mathbf{k}}^O]^{-1} \tilde{\varepsilon}_{\mathbf{k}}^{ONi} \tag{A.6c}$$

This assumes that the valence fluctuation on Oxygen can be relatively small compared to the onsite Coulomb repulsion, which is the usual case in most layered Nickelates.

Appendix B. Susceptibility

Appendix B.1. Non-interacting charge susceptibility

We define the charge susceptibility as the response function that measures the correlation between charge densities at different lattice sites. It is given by

$$\chi_{ij}(\tau)|_{\mathbf{c}} \equiv -\langle n_i(\tau) n_j(0) \rangle \tag{B.1}$$

where the charge density operator n_i is defined as

$$n_i = c_i^{\dagger\dagger} c_i^{\dagger} + c_i^{\dagger\dagger} c_i^{\dagger} - n \tag{B.2}$$

Here, $c_i^{\dagger\sigma}$ and c_i^σ are the Fermionic creation and annihilation operators, respectively, for spin σ at site i , and n is the average number of particles per site.

Expanding the correlation function, we have

$$\begin{aligned} \chi_{ij}(\tau)|_{\mathbf{c}} = & -\langle c_i^{\dagger\uparrow} c_i^\uparrow(\tau) c_j^{\dagger\uparrow} c_j^\uparrow(0) \rangle - \langle c_i^{\dagger\uparrow} c_i^\uparrow(\tau) c_j^{\dagger\downarrow} c_j^\downarrow(0) \rangle \\ & - \langle c_i^{\dagger\downarrow} c_i^\downarrow(\tau) c_j^{\dagger\uparrow} c_j^\uparrow(0) \rangle - \langle c_i^{\dagger\downarrow} c_i^\downarrow(\tau) c_j^{\dagger\downarrow} c_j^\downarrow(0) \rangle + n^2 \end{aligned} \quad (\text{B.3})$$

In the non-interacting case, we can apply Wick's theorem to express the four-point correlation functions as products of two-point correlation functions:

$$\begin{aligned} \chi_{ij}(\tau)|_{\mathbf{c}} = & -\langle c_i^{\dagger\uparrow}(\tau) c_j^\uparrow(0) \rangle \langle c_j^{\dagger\uparrow}(0) c_i^\uparrow(\tau) \rangle - \langle c_i^{\dagger\uparrow}(\tau) c_j^\downarrow(0) \rangle \langle c_j^{\dagger\downarrow}(0) c_i^\uparrow(\tau) \rangle \\ & - \langle c_i^{\dagger\downarrow}(\tau) c_j^\uparrow(0) \rangle \langle c_j^{\dagger\uparrow}(0) c_i^\downarrow(\tau) \rangle - \langle c_i^{\dagger\downarrow}(\tau) c_j^\downarrow(0) \rangle \langle c_j^{\dagger\downarrow}(0) c_i^\downarrow(\tau) \rangle \end{aligned} \quad (\text{B.4})$$

By introducing the Green's function $\mathcal{G}_{ij}^{\sigma\sigma'}(\tau)$, defined as

$$\mathcal{G}_{ij}^{\sigma\sigma'}(\tau) = -\langle T_\tau c_i^\sigma(\tau) c_j^{\dagger\sigma'}(0) \rangle \quad (\text{B.5})$$

where T_τ denotes time ordering in imaginary time, we can rewrite the charge susceptibility as

$$\begin{aligned} \chi_{ij}(\tau)|_{\mathbf{c}} = & -\mathcal{G}_{ij}^{\uparrow\uparrow}(\tau) \mathcal{G}_{ji}^{\uparrow\uparrow}(-\tau) - \mathcal{G}_{ij}^{\uparrow\downarrow}(\tau) \mathcal{G}_{ji}^{\downarrow\uparrow}(-\tau) \\ & - \mathcal{G}_{ij}^{\downarrow\uparrow}(\tau) \mathcal{G}_{ji}^{\uparrow\downarrow}(-\tau) - \mathcal{G}_{ij}^{\downarrow\downarrow}(\tau) \mathcal{G}_{ji}^{\downarrow\downarrow}(-\tau) \end{aligned} \quad (\text{B.6})$$

In the paramagnetic case, due to spin SU(2) symmetry, the Green's functions satisfy

$$\mathcal{G}_{ij}^{\sigma\sigma'} = \delta_{\sigma\sigma'} \mathcal{G}_{ij} \quad (\text{B.7})$$

where \mathcal{G}_{ij} is the spin-independent Green's function. Thus, the charge susceptibility simplifies to

$$\chi_{ij}(\tau)|_{\mathbf{c}} = -2\mathcal{G}_{ij}(\tau) \mathcal{G}_{ji}(-\tau) \quad (\text{B.8})$$

Appendix B.2. Non-interacting spin susceptibility

We define the transverse spin susceptibility as the correlation function for the transverse spin components, given by

$$\chi_{ij}^{+-}(\tau)|_{\mathbf{s}} \equiv -\langle \mathcal{S}_i^+(\tau) \mathcal{S}_j^-(0) \rangle \quad (\text{B.9})$$

where the spin raising operator \mathcal{S}_i^+ and spin lowering operator \mathcal{S}_i^- are defined as

$$\mathcal{S}_i^+ = c_i^{\dagger\uparrow} c_i^\downarrow, \quad \mathcal{S}_i^- = c_i^{\dagger\downarrow} c_i^\uparrow \quad (\text{B.10})$$

Therefore,

$$\begin{aligned} \chi_{ij}^{+-}(\tau)|_{\mathbf{s}} = & -\langle \mathcal{S}_i^+(\tau) \mathcal{S}_j^-(0) \rangle \\ = & -\langle c_i^{\dagger\uparrow} c_i^\downarrow(\tau) c_j^{\dagger\downarrow} c_j^\uparrow(0) \rangle \end{aligned} \quad (\text{B.11})$$

Using Wick's theorem,

$$\begin{aligned}\chi_{ij}^{+-}(\tau)|_s &= -\langle c_i^{\uparrow\dagger}(\tau)c_j^{\uparrow}(0)\rangle\langle c_j^{\dagger\downarrow}(0)c_i^{\downarrow}(\tau)\rangle \\ &= -\mathcal{G}_{ij}^{\uparrow\uparrow}(\tau)\mathcal{G}_{ji}^{\downarrow\downarrow}(-\tau)\end{aligned}\quad (\text{B.12})$$

Assuming the paramagnetic state (which implies $\mathcal{G}_{ij}^{\sigma\sigma'} = \delta_{\sigma\sigma'}\mathcal{G}_{ij}$ due to spin SU(2) symmetry), the spin susceptibility simplifies as follows:

$$\chi_{ij}^{+-}(\tau)|_s = -\mathcal{G}_{ij}(\tau)\mathcal{G}_{ji}(-\tau) \quad (\text{B.13})$$

Where, we define the Lindhard susceptibility as,

$$\chi_{0\ ij}(\tau) \equiv -\mathcal{G}_{ij}(\tau)\mathcal{G}_{ji}(-\tau) \quad (\text{B.14})$$

Thus, in the non-interacting paramagnetic case, the transverse spin susceptibility relates to the charge susceptibility as

$$\chi_{ij}^{+-}(\tau)|_s = \frac{1}{2}\chi_{ij}(\tau)|_c = \chi_{0\ ij}(\tau) \quad (\text{B.15})$$

Appendix B.3. Random Phase Approximation (RPA)

In the non-interacting case, we have derived the charge and spin susceptibilities, $\chi_{ij}(\tau)|_c$ and $\chi_{ij}^{+-}(\tau)|_s$, as functions of the non-interacting Green's function $\mathcal{G}_{ij}(\tau)$. However, when interactions are present, the susceptibilities are modified due to collective screening effects. The Random Phase Approximation (RPA) provides a way to account for these interaction effects perturbatively. Here, we will highlight some essential results from this well-known method for charge channel.

In the presence of interactions, the full susceptibility can be expressed in terms of the non-interacting susceptibility and the interaction potential. The interaction is typically modelled by a repulsive Coulomb interaction $V(\mathbf{q})|_c$ for the charge susceptibility. The full charge susceptibility χ_c^{RPA} is given by the RPA summation as:

$$\chi_{ij}^{RPA}(\tau)|_c = \chi_{0\ ij}(\tau) + V(\mathbf{q})|_c \sum_k \chi_{0\ ik}(\tau)\chi_{kj}^{RPA}(\tau)|_c \quad (\text{B.16})$$

Here, $\chi_{0\ ij}(\tau)$ is the non-interacting Lindhard susceptibility calculated earlier, and $V(\mathbf{q})|_c$ is the on-site Coulomb interaction.

In momentum space, this can be written as:

$$\chi^{RPA}(\mathbf{q}, i\omega_n)|_c = \frac{\chi_0(\mathbf{q}, i\omega_n)}{1 - V(\mathbf{q})|_c\chi_0(\mathbf{q}, i\omega_n)} \quad (\text{B.17})$$

where \mathbf{q} is the momentum and $i\omega_n$ is the Matsubara frequency. This expression describes how the interaction $V(\mathbf{q})|_c$ enhances the charge fluctuations. For full derivation, see Chapter 9. of [93]. It is to be noted that in the spin channel, the $V(\mathbf{q})|_s$ corresponds to a Heisenberg-type of exchange interaction instead of Coulomb interaction with a different sign.

Fits on <i>ab-initio</i> results:					
Compound	Ref	Orbitals	On-Site energy (eV)	NN hopping (eV)	NNN hopping (eV)
<i>LaNiO₂</i>	[46]	$Ni - d_{x^2-y^2}$	0.249	-0.368	0.099
<i>LaNiO₂</i>	[47]	$Ni - d_{x^2-y^2}$	0.093	-0.381	0.081
<i>LaNiO₂</i>	[48]	$Ni - d_{x^2-y^2}$	0.281	-0.380	0.088
		<i>Interstitial : s</i>	1.493	-0.031	-0.111
<i>LaNiO₂</i>	[49]	$Ni - d_{x^2-y^2}$	—	0.395	-0.095
<i>NdNiO₂</i>	[50]	$Ni - d_{x^2-y^2} + O - p_{x/y}$	—	0.254	-0.030
<i>LaNiO₂</i>	[51]	$Ni - d_{x^2-y^2}$	0.2689	-0.3894	0.0977
<i>NdNiO₂</i>		$Ni - d_{x^2-y^2}$	0.2502	-0.3974	0.0933
<i>LaNiO₂</i>	[15]	$Ni - d_{x^2-y^2}$	0.267	-0.355	—
		$La - d_{z^2}$	1.132	-0.164	—

Table C1

Compound	Ref	Orbital	NN-hopping (eV)	NNN-hopping (eV)	$\Delta_{d_{x^2-y^2}-d_{xy}}$ (eV)
$LaNiO_2$	[52]	$Ni-d_{x^2-y^2}$	-0.370	0.10	1.39
		$Ni-d_{xy}$	-0.16	-0.05	
$PrNiO_2$		$Ni-d_{x^2-y^2}$	-0.370	0.10	1.41
		$Ni-d_{xy}$	-0.16	-0.05	
$NdNiO_2$		$Ni-d_{x^2-y^2}$	-0.370	0.10	1.42
		$Ni-d_{xy}$	-0.16	-0.05	

Table C2

Compound	Ref.	Parameters (eV)				
<i>LaNiO₂</i>	[46]	$\tilde{\epsilon}_{2p}$	$\tilde{\epsilon}_{3d_{x^2-y^2}}$	$\tilde{\epsilon}_{3d_{z^2}}$	t_{pd}	t'_{pd}
		-5.41	-1.02	-1.73	-1.23	0.20
	[15]	$\tilde{\epsilon}_{2p}$	$\tilde{\epsilon}_{3d_{x^2-y^2}}$	$\tilde{\epsilon}_{3d_{z^2}}$	t_{pd}	t'_{pd}
		-3.26	0.70	0.04	-1.20	-0.30
		$\tilde{\epsilon}_{5d_z^2}$	t'_{dd}	t''_{dd}	t_{dd}	—
		-2.42	-0.5	—	—	—
	[20]	Δ_{dp}	$\tilde{\epsilon}_{3d_{x^2-y^2}}$	$\tilde{\epsilon}_{3d_{z^2}}$	$\tilde{\epsilon}_{5d_{z^2}}$	t'_{dd}
		-6	0.40	-2.94	2.649	0.253
<i>NdNiO₂</i>	[50]	Δ_{dp}	$\tilde{\epsilon}_{3d_{x^2-y^2}}$	t_{pd}	t_{pp}	—
		—	4.2	1.3	0.6	—

Table C3

Compound	Ref	Δ_{dp} (eV)	t_{pd} (eV)
<i>LaNiO₃</i>	[94]	4.4	-1.3

Table C4

Appendix C. Parameters

References

- [1] Shengwei Zeng, Chi Sin Tang, Xinmao Yin, Changjian Li, Mengsha Li, Zhen Huang, Junxiong Hu, Wei Liu, Ganesh Ji Omar, Hariom Jani, Zhi Shiuh Lim, Kun Han, Dongyang Wan, Ping Yang, Stephen John Pennycook, Andrew T. S. Wee, and Ariando Ariando. Phase Diagram and Superconducting Dome of Infinite-Layer $\text{Nd}_{1-x}\text{Sr}_x\text{NiO}_2$ Thin Films. *Phys. Rev. Lett.*, 125(14):147003, October 2020.
- [2] Shengwei Zeng, Changjian Li, Lin Er Chow, Yu Cao, Zhaoting Zhang, Chi Sin Tang, Xinmao Yin, Zhi Shiuh Lim, Junxiong Hu, Ping Yang, and Ariando Ariando. Superconductivity in infinite-layer Nickelate $\text{La}_{1-x}\text{Ca}_x\text{NiO}_2$ thin films. *Sci. Adv.*, 8(7), February 2022.
- [3] Motoki Osada, Bai Yang Wang, Kyuho Lee, Danfeng Li, and Harold Y. Hwang. Phase diagram of infinite layer praseodymium Nickelate $\text{Pr}_{1-x}\text{Sr}_x\text{NiO}_2$ thin films. *Phys. Rev. Mater.*, 4(12):121801, December 2020.
- [4] Motoki Osada, Bai Yang Wang, Berit H. Goodge, Shannon P. Harvey, Kyuho Lee, Danfeng Li, Lena F. Kourkoutis, and Harold Y. Hwang. Nickelate Superconductivity without Rare-Earth Magnetism: $(\text{La}, \text{Sr})\text{NiO}_2$. *Adv. Mater.*, 33(45):2104083, November 2021.
- [5] Danfeng Li, Kyuho Lee, Bai Yang Wang, Motoki Osada, Samuel Crossley, Hye Ryoung Lee, Yi Cui, Yasuyuki Hikita, and Harold Y. Hwang. Superconductivity in an infinite-layer Nickelate. *Nature*, 572:624–627, August 2019.
- [6] Danfeng Li, Bai Yang Wang, Kyuho Lee, Shannon P. Harvey, Motoki Osada, Berit H. Goodge, Lena F. Kourkoutis, and Harold Y. Hwang. Superconducting Dome in $\text{Nd}_{1-x}\text{Sr}_x\text{NiO}_2$ Infinite Layer Films. *Phys. Rev. Lett.*, 125(2):027001, July 2020.
- [7] Harrison LaBollita, Myung-Chul Jung, and Antia S. Botana. Many-body electronic structure of $d^{9-\delta}$ layered nickelates. *Phys. Rev. B*, 106(11):115132, September 2022.
- [8] Charles C. Tam, Jaewon Choi, Xiang Ding, Stefano Agrestini, Abhishek Nag, Mei Wu, Bing Huang, Huiqian Luo, Peng Gao, Mirian García-Fernández, Liang Qiao, and Ke-Jin Zhou. Charge density waves in infinite-layer NdNiO_2 Nickelates. *Nat. Mater.*, 21:1116–1120, October 2022.
- [9] C. T. Parzyck, N. K. Gupta, Y. Wu, V. Anil, L. Bhatt, M. Bouliane, R. Gong, B. Z. Gregory, A. Luo, R. Sutarto, F. He, Y.-D. Chuang, T. Zhou, G. Herranz, L. F. Kourkoutis, A. Singer, D. G. Schlom, D. G. Hawthorn, and K. M. Shen. Absence of 3a0 charge density wave order in the infinite-layer Nickelate NdNiO_2 . *Nat. Mater.*, 23:486–491, April 2024.
- [10] Lun-Hui Hu and Congjun Wu. Two-band model for magnetism and superconductivity in Nickelates. *Phys. Rev. Res.*, 1(3):032046, December 2019.
- [11] Jennifer Fowlie, Marios Hadjimichael, Maria M. Martins, Danfeng Li, Motoki Osada, Bai Yang Wang, Kyuho Lee, Yonghun Lee, Zaher Salman, Thomas Prokscha, Jean-Marc Triscone, Harold Y. Hwang, and Andreas Suter. Intrinsic magnetism in superconducting infinite-layer Nickelates. *Nat. Phys.*, 18:1043–1047, September 2022.
- [12] Ruby A. Shi, Bai Yang Wang, Yusuke Iguchi, Motoki Osada, Kyuho Lee, Berit H. Goodge, Lena F. Kourkoutis, Harold Y. Hwang, and Kathryn A. Moler. Scanning SQUID study of ferromagnetism and superconductivity in infinite-layer Nickelates. *Phys. Rev. Mater.*, 8(2):024802, February 2024.
- [13] M. Rossi, H. Lu, A. Nag, D. Li, M. Osada, K. Lee, B. Y. Wang, S. Agrestini, M. Garcia-Fernandez, J. J. Kas, Y.-D. Chuang, Z. X. Shen, H. Y. Hwang, B. Moritz, Ke-Jin Zhou, T. P. Devereaux, and W. S. Lee. Orbital and spin character of doped carriers in infinite-layer Nickelates. *Phys. Rev. B*, 104(22):L220505, December 2021.
- [14] Mi Jiang, Mona Berciu, and George A. Sawatzky. Critical Nature of the Ni Spin State in Doped NdNiO_2 . *Phys. Rev. Lett.*, 124(20):207004, May 2020.
- [15] M. Hepting, D. Li, C. J. Jia, H. Lu, E. Paris, Y. Tseng, X. Feng, M. Osada, E. Been, Y. Hikita, Y.-D. Chuang, Z. Hussain, K. J. Zhou, A. Nag, M. Garcia-Fernandez, M. Rossi, H. Y. Huang,

- D. J. Huang, Z. X. Shen, T. Schmitt, H. Y. Hwang, B. Moritz, J. Zaanen, T. P. Devereaux, and W. S. Lee. Electronic structure of the parent compound of superconducting infinite-layer Nickelates. *Nat. Mater.*, 19:381–385, April 2020.
- [16] Xiang Ding, Yu Fan, Xiaoxiao Wang, Chihao Li, Zhitong An, Jiahao Ye, Shenglin Tang, Minyinan Lei, Xingtian Sun, Nan Guo, Zhihui Chen, Suppanut Sangphet, Yilin Wang, Haichao Xu, Rui Peng, and Donglai Feng. Cuprate-like Electronic Structures in Infinite-Layer Nickelates with Substantial Hole Dopings. *Natl. Sci. Rev.*, page nwae194, June 2024.
- [17] Wenjie Sun, Zhicheng Jiang, Chengliang Xia, Bo Hao, Yueying Li, Shengjun Yan, Maosen Wang, Hongquan Liu, Jianyang Ding, Jiayu Liu, Zhengtai Liu, Jishan Liu, Hanghui Chen, Dawei Shen, and Yuefeng Nie. Electronic Structure of Superconducting Infinite-Layer Lanthanum Nickelates. *arXiv*, March 2024.
- [18] Qiangqiang Gu, Yueying Li, Siyuan Wan, Huazhou Li, Wei Guo, Huan Yang, Qing Li, Xiyu Zhu, Xiaoqing Pan, Yuefeng Nie, and Hai-Hu Wen. Single particle tunneling spectrum of superconducting $\text{Nd}_{1-x}\text{Sr}_x\text{NiO}_2$ thin films. *Nat. Commun.*, 11(6027):1–7, November 2020.
- [19] Hirofumi Sakakibara, Hidetomo Usui, Katsuhiko Suzuki, Takao Kotani, Hideo Aoki, and Kazuhiko Kuroki. Model Construction and a Possibility of Cupratelike Pairing in a New d^9 Nickelate Superconductor $(\text{Nd}, \text{Sr})\text{NiO}_2$. *Phys. Rev. Lett.*, 125(7):077003, August 2020.
- [20] Peiheng Jiang, Liang Si, Zhaoliang Liao, and Zhicheng Zhong. Electronic structure of rare-earth infinite-layer $R\text{NiO}_2$ ($R = \text{La}, \text{Nd}$). *Phys. Rev. B*, 100(20):201106, November 2019.
- [21] Emily Been, Wei-Sheng Lee, Harold Y. Hwang, Yi Cui, Jan Zaanen, Thomas Devereaux, Brian Moritz, and Chunjing Jia. Electronic structure trends across the rare-earth series in superconducting infinite-layer nickelates. *Phys. Rev. X*, 11:011050, Mar 2021.
- [22] Antia S. Botana, Kwan-Woo Lee, Michael R. Norman, Victor Pardo, and Warren E. Pickett. Low Valence Nickelates: Launching the Nickel Age of Superconductivity. *Front. Phys.*, 9:813532, February 2022.
- [23] Frank Lechermann. Multiorbital Processes Rule the $\text{Nd}_{1-x}\text{Sr}_x\text{NiO}_2$ Normal State. *Phys. Rev. X*, 10(4):041002, October 2020.
- [24] Frank Lechermann. Emergent flat-band physics in $d^{9-\delta}$ multilayer Nickelates. *Phys. Rev. B*, 105(15):155109, April 2022.
- [25] M. Medarde. Structural, magnetic and electronic properties of perovskites $R\text{NiO}_3$ ($R = \text{rare earth}$). *J. Phys.: Condens. Matter*, 1997.
- [26] C. Piamonteze, H. C. N. Tolentino, A. Y. Ramos, N. E. Massa, J. A. Alonso, M. J. Martínez-Lope, and M. T. Casais. Structural changes in $R\text{NiO}_3$ perovskites ($R = \text{rare earth}$) across the metal–insulator transition. *Physica B*, 320(1):71–74, July 2002.
- [27] J. A. Alonso, M. J. Martínez-Lope, J. L. García-Muñoz, and M. T. Fernández. Crystal structure and magnetism in the defect perovskite $\text{lanio}_{2.5}$. *Physica B: Condensed Matter*, 234-236:18–19, 1997.
- [28] J. L. García-Muñoz, J. Rodríguez-Carvajal, and P. Lacorre. Neutron-diffraction study of the magnetic ordering in the insulating regime of the perovskites $R\text{NiO}_3$ ($R = \text{Pr}$ and Nd). *Phys. Rev. B*, 50(2):978–992, July 1994.
- [29] Valentina Bisogni, Sara Catalano, Robert J. Green, Marta Gibert, Raoul Scherwitzl, Yaobo Huang, Vladimir N. Strocov, Pavlo Zubko, Shadi Balandeh, Jean-Marc Triscone, George Sawatzky, and Thorsten Schmitt. Ground-state Oxygen holes and the metal–insulator transition in the negative charge-transfer rare-earth Nickelates. *Nat. Commun.*, 7(13017):1–8, October 2016.
- [30] Julien Varignon, Mathieu N. Grisolia, Jorge Íñiguez, Agnès Barthélémy, and Manuel Bibes. Complete phase diagram of rare-earth Nickelates from first-principles. *npj Quantum Mater.*, 2(21):1–9, April 2017.
- [31] T. Mizokawa, H. Namatame, A. Fujimori, K. Akeyama, H. Kondoh, H. Kuroda, and N. Kosugi. Origin of the band gap in the negative charge-transfer-energy compound NaCuO_2 . *Phys. Rev. Lett.*, 67(12):1638–1641, September 1991.
- [32] Susumu Yamamoto and Takeo Fujiwara. Charge and Spin Order in $R\text{NiO}_3$ ($R = \text{Nd}, \text{Y}$) by

- LSDA+U Method. *J. Phys. Soc. Jpn.*, 71(5):1226–1229, May 2002.
- [33] Yi Lu, Zhicheng Zhong, Maurits W. Haverkort, and Philipp Hansmann. Origins of bond and spin order in rare-earth Nickelate bulk and heterostructures. *Phys. Rev. B*, 95(19):195117, May 2017.
 - [34] Jong-Woo Kim, Yongseong Choi, S. Middey, D. Meyers, J. Chakhalian, Padraic Shafer, H. Park, and Philip J. Ryan. Direct Evidence of the Competing Nature between Electronic and Lattice Breathing Order in Rare-Earth Nickelates. *Phys. Rev. Lett.*, 124(12), March 2020.
 - [35] G. Krieger, L. Martinelli, S. Zeng, L. E. Chow, K. Kummer, R. Arpaia, M. Moretti Sala, N. B. Brookes, A. Ariando, N. Viart, M. Salluzzo, G. Ghiringhelli, and D. Preziosi. Charge and Spin Order Dichotomy in $NdNiO_2$ Driven by the Capping Layer. *Phys. Rev. Lett.*, 129(2):027002, July 2022.
 - [36] Xiaolin Ren, Ronny Sutarto, Qiang Gao, Qisi Wang, Jiarui Li, Yao Wang, Tao Xiang, Jiangping Hu, J. Chang, Riccardo Comin, X. J. Zhou, and Zhihai Zhu. Two Distinct Charge Orders in Infinite-layer $PrNiO_{2+\delta}$ revealed by Resonant X-ray Diffraction. *arXiv*, March 2023.
 - [37] Ruiqi Zhang, Christopher Lane, Johannes Nokelainen, Bahadur Singh, Bernardo Barbiellini, Robert S. Markiewicz, Arun Bansil, and Jianwei Sun. Emergence of Competing Stripe Phases in Undoped Infinite-Layer Nickelates. *Phys. Rev. Lett.*, 133(6):066401, August 2024.
 - [38] Christopher Lane, Ruiqi Zhang, Bernardo Barbiellini, Robert S. Markiewicz, Arun Bansil, Jianwei Sun, and Jian-Xin Zhu. Competing incommensurate spin fluctuations and magnetic excitations in infinite-layer nickelate superconductors. *Commun. Phys.*, 6(90):1–11, May 2023.
 - [39] Yang Zhang, Ling-Fang Lin, Adriana Moreo, Thomas A. Maier, and Elbio Dagotto. Trends in electronic structures and s_{\pm} -wave pairing for the rare-earth series in bilayer Nickelate superconductor $R_3Ni_2O_7$. *Phys. Rev. B*, 108(16):165141, October 2023.
 - [40] R. S. Dhaka, Tanmoy Das, N. C. Plumb, Z. Ristic, W. Kong, C. E. Matt, N. Xu, Kapildeb Dolui, E. Razzoli, M. Medarde, L. Patthey, M. Shi, M. Radović, and Joël Mesot. Tuning the metal-insulator transition in $NdNiO_3$ heterostructures via Fermi surface instability and spin fluctuations. *Phys. Rev. B*, 92(3):035127, July 2015.
 - [41] P. D. C. King, H. I. Wei, Y. F. Nie, M. Uchida, C. Adamo, S. Zhu, X. He, I. Božović, D. G. Schlom, and K. M. Shen. Atomic-scale control of competing electronic phases in ultrathin $LaNiO_3$. *Nat. Nanotechnol.*, 9:443–447, June 2014.
 - [42] Simone Di Cataldo, Paul Worm, Jan M. Tomczak, Liang Si, and Karsten Held. Unconventional superconductivity without doping in infinite-layer nickelates under pressure. *Nat. Commun.*, 15(3952):1–6, May 2024.
 - [43] Liang Si, Eric Jacob, Wenfeng Wu, Andreas Hausoel, Juraj Krsnik, Paul Worm, Simone Di Cataldo, Oleg Janson, and Karsten Held. Closing in on possible scenarios for infinite-layer nickelates: comparison of dynamical mean-field theory with angular-resolved photoemission spectroscopy. *arXiv*, August 2024.
 - [44] Yuhao Gu, Sichen Zhu, Xiaoxuan Wang, Jiangping Hu, and Hanghui Chen. A substantial hybridization between correlated Ni-d orbital and itinerant electrons in infinite-layer nickelates. *Commun. Phys.*, 3(84):1–9, May 2020.
 - [45] Hanghui Chen, Yi-feng Yang, Guang-Ming Zhang, and Hongquan Liu. An electronic origin of charge order in infinite-layer nickelates. *Nat. Commun.*, 14(5477):1–11, September 2023.
 - [46] A. S. Botana and M. R. Norman. Similarities and differences between $LaNiO_2$ and $CaCuO_2$ and implications for superconductivity. *Phys. Rev. X*, 10:011024, Feb 2020.
 - [47] K.-W. Lee and W. E. Pickett. Infinite-layer $LaNiO_2$: Ni^{1+} is not Cu^{2+} . *Phys. Rev. B*, 70(16):165109, October 2004.
 - [48] Tharathep Plienbumrung, Maria Daghofer, Michael Schmid, and Andrzej M. Oleś. Screening in a two-band model for superconducting infinite-layer Nickelate. *Phys. Rev. B*, 106(13):134504, October 2022.
 - [49] Marcel Klett, Philipp Hansmann, and Thomas Schäfer. Magnetic Properties and Pseudogap Formation in Infinite-Layer Nickelates: Insights From the Single-Band Hubbard Model. *Front. Phys.*, 10:834682, February 2022.

- [50] Hu Zhang, Lipeng Jin, Shanmin Wang, Bin Xi, Xingqiang Shi, Fei Ye, and Jia-Wei Mei. Effective Hamiltonian for Nickelate oxides $\text{Nd}_{1-x}\text{Sr}_x\text{NiO}_2$. *Phys. Rev. Res.*, 2(1):013214, February 2020.
- [51] Motoharu Kitatani, Liang Si, Oleg Janson, Ryotaro Arita, Zhicheng Zhong, and Karsten Held. Nickelate superconductors—a renaissance of the one-band Hubbard model. *npj Quantum Mater.*, 5(59):1–6, August 2020.
- [52] T. Y. Xie, Z. Liu, Chao Cao, Z. F. Wang, J. L. Yang, and W. Zhu. Microscopic theory of superconducting phase diagram in infinite-layer Nickelates. *Phys. Rev. B*, 106(3):035111, July 2022.
- [53] Qiangqiang Gu and Hai-Hu Wen. Superconductivity in Nickel-based 112 systems. *Innovation*, 3(1):100202, January 2022.
- [54] Yusuke Nomura and Ryotaro Arita. Superconductivity in infinite-layer Nickelates. *Rep. Prog. Phys.*, 85(5):052501, March 2022.
- [55] Bai Yang Wang, Kyuho Lee, and Berit H. Goodge. Experimental Progress in Superconducting Nickelates. *Annu. Rev. Condens. Matter Phys.*, (Volume 15, 2024):305–324, March 2024.
- [56] Y. Wang, C.-J. Kang, H. Miao, and G. Kotliar. Hund’s metal physics: From SrNiO_2 to LaNiO_2 . *Phys. Rev. B*, 102(16):161118, October 2020.
- [57] Guang-Ming Zhang, Yi-feng Yang, and Fu-Chun Zhang. Self-doped Mott insulator for parent compounds of Nickelate superconductors. *Phys. Rev. B*, 101(2):020501, January 2020.
- [58] Xianxin Wu, Domenico Di Sante, Tilman Schwemmer, Werner Hanke, Harold Y. Hwang, Srinivas Raghu, and Ronny Thomale. Robust $d_{x^2-y^2}$ -wave superconductivity of infinite-layer Nickelates. *Phys. Rev. B*, 101(6):060504, February 2020.
- [59] Mi-Young Choi, Kwan-Woo Lee, and Warren E. Pickett. Role of $4f$ states in infinite-layer NdNiO_2 . *Phys. Rev. B*, 101:020503, Jan 2020.
- [60] Yusuke Nomura, Motoaki Hirayama, Terumasa Tadano, Yoshihide Yoshimoto, Kazuma Nakamura, and Ryotaro Arita. Formation of a two-dimensional single-component correlated electron system and band engineering in the Nickelate superconductor NdNiO_2 . *Phys. Rev. B*, 100(20):205138, November 2019.
- [61] Karsten Held, Liang Si, Paul Worm, Oleg Janson, Ryotaro Arita, Zhicheng Zhong, Jan M. Tomczak, and Motoharu Kitatani. Phase Diagram of Nickelate Superconductors Calculated by Dynamical Vertex Approximation. *Front. Phys.*, 9:810394, January 2022.
- [62] Frank Lechermann. Late transition metal oxides with infinite-layer structure: Nickelates versus cuprates. *Phys. Rev. B*, 101(8):081110, February 2020.
- [63] Andreas Kreisel, Brian M. Andersen, Astrid T. Rømer, Ilya M. Eremin, and Frank Lechermann. Superconducting Instabilities in Strongly Correlated Infinite-Layer Nickelates. *Phys. Rev. Lett.*, 129(7):077002, August 2022.
- [64] Philipp Werner and Shintaro Hoshino. Nickelate superconductors: Multiorbital nature and spin freezing. *Phys. Rev. B*, 101(4):041104, January 2020.
- [65] JJ Zuckerman. Crystal field splitting diagrams. *Journal of Chemical Education*, 42(6):315, 1965.
- [66] Yusuke Nomura, Takuya Nomoto, Motoaki Hirayama, and Ryotaro Arita. Magnetic exchange coupling in cuprate-analog d^9 nickelates. *Phys. Rev. Res.*, 2(4):043144, October 2020.
- [67] Alexandru B. Georgescu, Oleg E. Peil, Ankit S. Disa, Antoine Georges, and Andrew J. Millis. Disentangling lattice and electronic contributions to the metal–insulator transition from bulk vs. layer confined RNiO_3 . *Proc. Natl. Acad. Sci. U.S.A.*, 116(29):14434–14439, July 2019.
- [68] Andreas Rüegg, Chandrima Mitra, Alexander A. Demkov, and Gregory A. Fiete. Electronic structure of $(\text{LaNiO}_3)_2/(\text{LaAlO}_3)_N$ heterostructures grown along [111]. *Phys. Rev. B*, 85:245131, Jun 2012.
- [69] Jian Liu, Mehdi Kargarian, Mikhail Kareev, Ben Gray, Phil J. Ryan, Alejandro Cruz, Nadeem Tahir, Yi-De Chuang, Jinghua Guo, James M. Rondinelli, et al. Heterointerface engineered electronic and magnetic phases of NdNiO_3 thin films. *Nat. Commun.*, 4(2714):1–11, November 2013.
- [70] J.-S. Zhou, J. B. Goodenough, and B. Dabrowski. Exchange Interaction in the Insulating Phase

- of RNiO_3 . *Phys. Rev. Lett.*, 95:127204, Sep 2005.
- [71] Electronic structure and magnetism in infinite-layer Nickelates RNiO_2 ($R = \text{La-Lu}$), author = Kapeghian, Jesse and Botana, Antia S. *Phys. Rev. B*, 102:205130, Nov 2020.
 - [72] Tharathep Plienbumrung, Maria Daghofer, and Andrzej M. Oleś. Interplay between Zhang-Rice singlets and high-spin states in a model for doped NiO_2 planes. *Phys. Rev. B*, 103(10):104513, March 2021.
 - [73] Zhen Fan, Jian-Feng Zhang, Bo Zhan, Dingshun Lv, Xing-Yu Jiang, Bruce Normand, and Tao Xiang. Superconductivity in nickelate and cuprate superconductors with strong bilayer coupling. *Phys. Rev. B*, 110(2):024514, July 2024.
 - [74] A. S. Botana and M. R. Norman. Similarities and Differences between LaNiO_2 and CaCuO_2 and Implications for Superconductivity. *Phys. Rev. X*, 10(1):011024, February 2020.
 - [75] Henrik Smith. The Lindhard Function and the Teaching of Solid State Physics. *Phys. Scr.*, 28(3):287, September 1983.
 - [76] Chao Chen, Runyu Ma, XueLei Sui, Ying Liang, Bing Huang, and Tianxing Ma. Antiferromagnetic fluctuations and dominant d_{xy} -wave pairing symmetry in Nickelate-based superconductors. *Phys. Rev. B*, 106(19):195112, November 2022.
 - [77] Tao Zhou, Yi Gao, and ZiDan Wang. Spin excitations in Nickelate superconductors. *Sci. China Phys. Mech. Astron.*, 63(8):1–9, August 2020.
 - [78] Fangze Liu, Cheng Peng, Edwin W. Huang, Brian Moritz, Chunjing Jia, and Thomas P. Devereaux. Emergence of antiferromagnetic correlations and Kondolike features in a model for infinite layer Nickelates. *npj Quantum Mater.*, 9(49):1–7, June 2024.
 - [79] A. A. Vladimirov, D. Ihle, and N. M. Plakida. Dynamic spin susceptibility of superconducting Cuprates: A microscopic theory of the magnetic resonance mode. *Phys. Rev. B*, 83(2):024411, January 2011.
 - [80] Y. Sidis, S. Pailhès, B. Keimer, P. Bourges, C. Ulrich, and L. P. Regnault. Magnetic resonant excitations in High-Tc superconductors. *Phys. Status Solidi B*, 241(6):1204–1210, May 2004.
 - [81] Yvan Sidis, Stéphane Pailhès, Vladimir Hinkov, Benoît Fauqué, Clemens Ulrich, Lucia Capogna, Alexandre Ivanov, Louis-Pierre Regnault, Bernhard Keimer, and Philippe Bourges. Inelastic neutron scattering study of spin excitations in the superconducting state of high temperature superconductors. *C. R. Phys.*, 8(7-8):745–762, 2007.
 - [82] Matthias Eschrig. The effect of collective spin-1 excitations on electronic spectra in high- Tc superconductors. *Adv. Phys.*, January 2006.
 - [83] Qimiao Si, Yuyao Zha, K. Levin, and J. P. Lu. Comparison of spin dynamics in $\text{YBa}_2\text{Cu}_3\text{O}_{7-\delta}$ and $\text{La}_{2-x}\text{Sr}_x\text{CuO}_4$: Effects of Fermi-surface geometry. *Phys. Rev. B*, 47(14):9055–9076, April 1993.
 - [84] H. F. Fong, P. Bourges, Y. Sidis, L. P. Regnault, J. Bossy, A. Ivanov, D. L. Milius, I. A. Aksay, and B. Keimer. Spin susceptibility in underdoped $\text{YBa}_2\text{Cu}_3\text{O}_{6+x}$. *Phys. Rev. B*, 61(21):14773–14786, June 2000.
 - [85] Pengcheng Dai, H. A. Mook, R. D. Hunt, and F. Doğan. Evolution of the resonance and incommensurate spin fluctuations in superconducting $\text{YBa}_2\text{Cu}_3\text{O}_{6+x}$. *Phys. Rev. B*, 63(5):054525, January 2001.
 - [86] Hiroyuki Yamase and Walter Metzner. Magnetic excitations and their anisotropy in $\text{YBa}_2\text{Cu}_3\text{O}_{6+x}$: Slave-boson mean-field analysis of the bilayer t - J model. *Phys. Rev. B*, 73(21):214517, June 2006.
 - [87] Navinder Singh. Leading theories of the Cuprate superconductivity: A critique. *Phys. C*, 580:1353782, January 2021.
 - [88] Hualei Sun, Mengwu Huo, Xunwu Hu, Jingyuan Li, Zengjia Liu, Yifeng Han, Lingyun Tang, Zhongquan Mao, Pengtao Yang, Bosen Wang, Jinguang Cheng, Dao-Xin Yao, Guang-Ming Zhang, and Meng Wang. Signatures of superconductivity near 80 K in a nickelate under high pressure. *Nature*, 621:493–498, September 2023.
 - [89] Siheon Ryee, Niklas Witt, and Tim O. Wehling. Quenched Pair Breaking by Interlayer Correlations

- as a Key to Superconductivity in $\text{La}_3\text{Ni}_2\text{O}_7$. *Phys. Rev. Lett.*, 133(9):096002, August 2024.
- [90] N. N. Wang, M. W. Yang, Z. Yang, K. Y. Chen, H. Zhang, Q. H. Zhang, Z. H. Zhu, Y. Uwatoko, L. Gu, X. L. Dong, J. P. Sun, K. J. Jin, and J.-G. Cheng. Pressure-induced monotonic enhancement of T_c to over 30 K in superconducting $\text{Pr}_{0.82}\text{Sr}_{0.18}\text{NiO}_2$ thin films. *Nat. Commun.*, 13(4367):1–8, July 2022.
 - [91] SungBin Lee, Ru Chen, and Leon Balents. Metal-insulator transition in a two-band model for the perovskite nickelates. *Phys. Rev. B*, 84(16):165119, October 2011.
 - [92] Yong Zhong, Kyuho Lee, Regan Bhatta, Yonghun Lee, Martin Gonzalez, Jiarui Li, Ruohan Wang, Makoto Hashimoto, Donghui Lu, Sung-Kwan Mo, Chunjing Jia, Harold Y. Hwang, and Zhi-Xun Shen. Electronically Amplified Electron-Phonon Interaction and Metal-Insulator Transition in Perovskite Nickelates. *arXiv*, July 2024.
 - [93] Henrik Bruus and Karsten Flensberg. *Many-body quantum theory in condensed matter physics: an introduction*. OUP Oxford, 2004.
 - [94] Alejandro Lopez-Bezanilla, Louis-François Arsenault, Anand Bhattacharya, Peter B. Littlewood, and Andrew J. Millis. Parameter transferability, self-doping, and metallicity in $\text{LaNiO}_3/\text{LaMnO}_3$ superlattices. *Phys. Rev. B*, 99(3):035133, January 2019.